CHALMERS
UNIVERSITY OF TECHNOLOGY

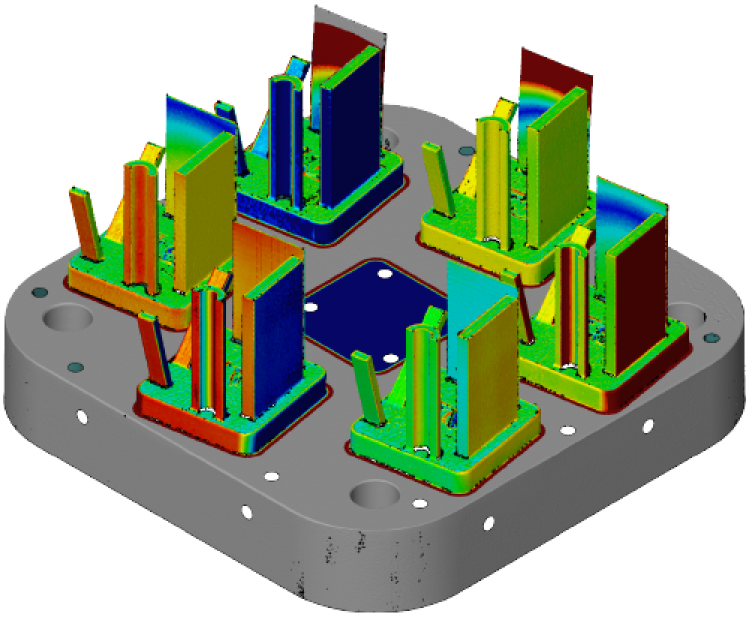

The Effect of Scanning Strategies on Geometrical Accuracy & Surface Roughness of H13 Tool Steel Parts in Laser Powder Bed Fusion Process

Master's thesis in Materials Engineering
Master's thesis in Product Development

MASOUD AHMADNIA FEIZABADI
ASHOK KUMAR RAJENDRAN

Department of Industrial and Materials Science
CHALMERS UNIVERSITY OF TECHNOLOGY
Gothenburg, Sweden 2019

Master's thesis 2019:NN

The Effect of Scanning Strategies on Geometrical Accuracy & Surface Roughness of H13 Tool Steel Parts in Laser Powder Bed Fusion Process

MASOUD AHMADNIA FEIZABADI
ASHOK KUMAR RAJENDERAN

Department of Industrial and Materials Science
Division of Product Development
Geomtery Assurance and Robust Design
Chalmers University of Technology
Gothenburg, Sweden 2019

The Effect of Scanning Strategies on Geometrical Accuracy & Surface Roughness of H13 Tool Steel Parts in Laser Powder Bed Fusion Process

MASOUD AHMADNIA FEIZABADI

ASHOK KUMAR RAJENDRAN

Supervisor: Johan Berglund, RISE IVF
Supervisor: Vaishak Ramesh Sagar, Chalmers University of Technology
Examiner:Kristina Wäremfjord, Department of Industrial and Materials Science

Master's Thesis 2019:NN
Department of Industrial and Materials Science
Division of Product Development
Geomtery Assurance & Robust Design
Chalmers University of Technology
SE-412 96 Gothenburg
Telephone +46 31 772 1000

Cover: 3D scanned mesh of the 3D printed artifact superimposed on the CAD model, produced by GOM Inspect.

Printed by Chalmers Reproservice
Gothenburg, Sweden 2019

The Effect of Scanning Strategies on Geometrical Accuracy & Surface Roughness of H13 Tool Steel Parts in Laser Powder Bed Fusion Process

MASOUD AHMADNIA FEIZABADI
ASHOK KUMAR RAJENDRAN
Department of Industrial and Materials Science
Chalmers University of Technology

Abstract

Additive Manufacturing (AM) combined with the development of new materials and the current available processes, has the potential to revolutionize the way of manufacturing products. Making parts with higher geometrical precision and better surface finish will pace up this revolution. In this project the effect of scanning strategies on geometrical accuracy and surface roughness of parts made of H13 tool steel via SLM process is investigated. A raster scanning pattern with 3 different hatch rotation angles(10, 67 and 180 degrees) were implemented. The effect of contouring was also studied by comparing the results from contoured and non-contoured samples. The results show that the 10 degree hatch rotation angle causes less deviation even though 67 degree is commonly mentioned as the optimum hatch rotation angle in most of the research papers. The surface roughness in parts printed without the contouring step is of poorer quality than the ones with contouring. Irrespective of employing this contouring step or not, a post-processing step like milling or grinding is required to achieve the desired surface roughness. Therefore, it can be suggested to skip contouring in order to save printing time. However, in terms of achieving the best geometrical accuracy, it is recommended that the contouring step is employed for printing thin wall of 0.5mm thick.

Keywords: SLM, Geometry Assurance, Surface Roughness, Scanning Strategy, Contouring, Hatch Rotation Angle

Acknowledgements

We would like to express our deepest gratitude to Johan Berglund, RISE IVF who have given us this opportunity to conduct our Master's thesis. Many thanks to our supervisor from Chalmers University of Technology, Vaishak Ramesh Sagar who has guided and supported us throughout our thesis work. Special thanks to our examiner Kristina Wärmefjord, for the continuous guidance. We would like to thank David Ohlsson, Sebastian Proper, Anton Dahl-Jendelin & Lars-Olof Ingemarsson, RISE IVF for their help in various stages of our thesis.
A special mention to the Centre of Additive Manufacturing (CAM2). The work was performed in the framework of the Centre for Additive Manufacturing – Metal (CAM2), supported by Vinnova."

Masoud Ahmadnia Feizabadi, Ashok Kumar Rajendran, Gothenburg, August 2019

Contents

List of Figures

List of Tables

List of Abbreviations

ALM	Additive Layer manufacturing
AM	Additive Manufacturing
ASME	American Society of Mechanical Engineering
CAD	Computer Aided Design
CAE	Computer Aided Engineering
CAM2	Center of Additive Manufacturing-Metal
CSI	Coherence Scanning Interferometry
FV	Focus Variation
FEA	Finite Element Analysis
GD&T	Geometrical Dimensioning and Tolerances
ICM	Imaging Confocal Microscopy
L-PBF	Laser Powder Bed Fusion
PBF	Powder Bed Fusion
PSD	Particle Size Distribution
RQ	Research Question
SEM	Scanning Electron Microscopy
SLM	Selective Laser Melting
SSF	Stress Scaling Factor
TGM	Temperature Gradient Mechanism

1
Introduction

1.1 Background

Additive Manufacturing (AM) combined with the development of new materials and the currently available processes, has the potential to revolutionize the way of manufacturing products. This technology is rapidly expanding in the recent times and it has found extensive application in aerospace, automotive industry and bio implants. This can be attributed to the fact that AM has many advantages in terms of design freedom, weight reduction, high mechanical performance due to special micro-structure and producing nearly finished parts which reduces the production lead time. On the other hand, the physical phenomena of metal AM is not perfectly understood yet. Though many parameters have found to be significant on the micro-structure and topology of the product, surface roughness and geometrical inaccuracies are two prominent obstacles that hinder faster growth of this technology. The surfaces of metal AM parts are drastically rough compared to parts produced using conventional manufacturing methods due to many reasons, one of them being the layer by layer nature of this process and the final product dimensions might be beyond the designed tolerances. Therefore, an additional post processing step is required to decrease the surface roughness and make the part in desired dimensions. Extensive research has been conducted to investigate the significant parameters in L-PBF which affects the final characteristics of metal AM products. However, the effect of scanning strategies including pattern type, size, orientation angle, re-melting and contouring strategies on the surface roughness and geometrical accuracy is rarely discussed yet.

1.2 Aim

The aim of this project is to investigate the effect of scanning strategies on geometrical accuracy and surface roughness for H13 Tool Steel parts made in L-PBF.

1.3 Limitations

There are many input parameters which might affect the surface topology and geometry of the products. For instance, material and powder specifications such as particle size distribution (PSD) and allotropic transformation of material below the melting point may affect the surface roughness and residual stresses accordingly,

which lead to more geometry inaccuracies. Hence, it is important to limit the parameters to investigate. In this project,
1. The focus is only on the effect of scanning and contouring strategies. Although other parameters might have interactions, they are being kept constant in this project.
2. The thesis will not cover the analysis of micro-structural effects and residual stresses. In addition, the effect of machine capabilities in terms of geometrical accuracy is not studied since we limit our printings to one machine.
3. This project is limited only to L-PBF as it will be difficult to translate the results from this project to a similar AM process like Electron Beam Melting.
4. The experiments will be conducted only on one material, which is H13 Tool Steel.

1.4 Research Questions

Few studies are conducted on the effect of L-PBF parameters on the surface roughness and geometrical accuracy of metal parts. They do not provide a clear protocol because most of them have been carried out to study the residual stresses of printed parts. While it has been detected that scan strategies (hatch rotation angle, scan pattern and size) influence the level and distribution of residual stresses; study of the effect of these parameters on the surface roughness and geometrical variation is hardly found among recent papers. This thesis work aims to answer these questions regarding geometry assurance and surface roughness:
RQ 1: Which hatch rotation angle is optimum?
RQ 2: Is contouring required?
RQ 3: Does hatch rotation angle have an effect on surface roughness?

2

Theory

This chapter covers the literature about the geometrical deviation and surface roughness in parts produced via L-PBF process.The background information related to L-PBF and other equipment used in this project are also mentioned in subsections. The theory related to the L-PBF process simulations is included at the end of this chapter.

2.1 Laser-Powder Bed Fusion

L-PBF is a layer by layer additive manufacturing process which selectively melts the powder bed. This process is repeated till the desired part dimensions are achieved. The construction of the part takes place inside a chamber that is completely enclosed and filled with an inert gas like argon in order to reduce oxidation of the powder. In some cases, the temperature of the powder in the build platform is elevated to just below the melting point. This process is carried out to minimize the laser power requirements and to prevent distortions in the part due to non-uniform thermal expansion and contraction. During the laser melting process, a layer of metal powder is applied with the help of a re-coater blade. The laser beam will selectively melt the powder layer. The metal powder partially absorbs the laser which creates a melt pool and solidifies rapidly. Then the platform is lowered by the prescribed layer thickness value which ranges from 20µm to 120µm and subsequently a new layer of powder is added using the re-coater blade. This laser melting process is repeated for a few thousand cycles until the part reaches the desired height[1]

2.1.1 Process Parameters

Any manufacturing process contains a number of parameters that affect the outcome of the produced part. In L-PBF there are a variety of process parameters that can affect a part in different ways. Considering that L-PBF is a very young process, many of these parameters and their effect on the parts need to be understood. It is important to know that the parameters are extremely inter-dependent and mutually interacting with each other. The four main categories of process parameters in L-PBF are: [2]

- Laser related parameters:
  - Laser Power
  - Spot size
  - Pulse duration

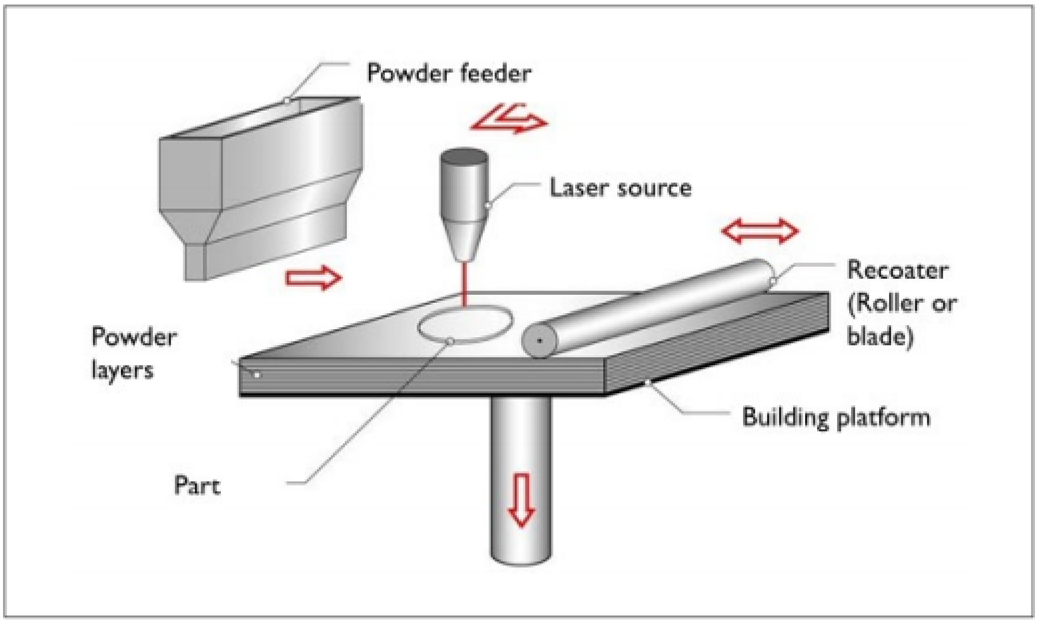

Figure 2.1: Schematic of a L-PBF process[3]

  - Pulse frequency
- Scan related parameters:
  - Scan speed
  - Scan spacing
  - Scan pattern
- Powder related parameters:
  - Particle shape
  - Particle size and distribution
  - Powder bed density
  - Layer thickness
  - Material properties
- Temperature related parameters:
  - Powder Bed Temperature
  - Temperature Distribution

Apart from the above-mentioned process parameters; there are other influencing factors that must be considered during part production. For instance, calibration of the machine has to be done properly since the machines behave differently with various manufacturers even though the technology is similar.

2.1.1.1 Laser-related Parameters

Most L-PBF processes used continuous-wave (CW) lasers. However, there is extensive research being conducted on pulsed laser. A pulsed energy is preferred because it has the tendency to form disconnected balls of molten metal, rather than a flat molten region on a powder bed surface. Laser power, spot size, scan speed and bed temperature, when combined, determines the energy input needed to fuse the powder into a usable part. The longer the laser dwells in a particular location, the deeper

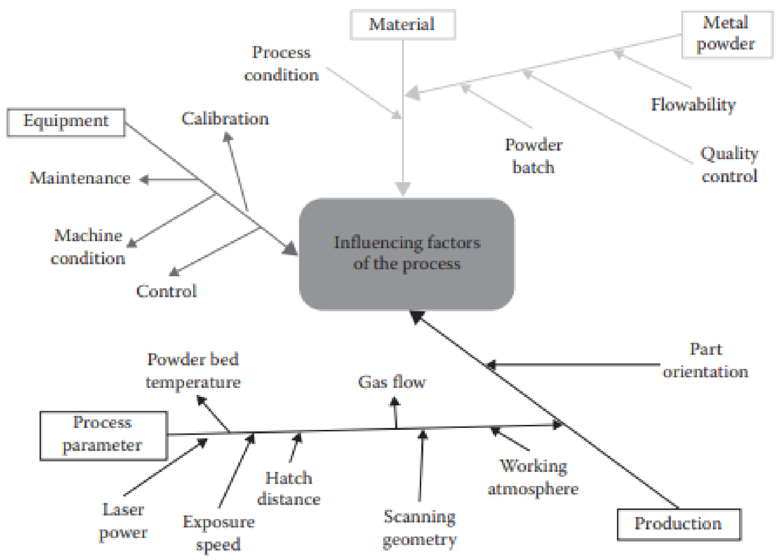

Figure 2.2: Main overview of the influencing factors in L-PBF[1]

the fusion depth and larger the melt pool diameter. Scan spacing is dependent on the laser power as it must ensure a sufficient degree of melt pool overlap between adjacent lines of fused material so that robust mechanical properties are achieved. The characteristics of a melt pool and its formation is basically determined by the total amount of energy applied which is absorbed by the powder bed as the laser beam scans. Both the melt pool size and the depth are a function of absorbed energy density. Since there are many parameters influencing this energy density, a simplified model has been formulated to calculate the energy density. Equation 2.1 is used to calculate the energy density.

$$E = \frac{P}{V * H * T} \tag{2.1}$$

Where; E= Energy Density in J/cu. mm

P = Laser Power in W

V = Scanning Speed in mm/s

H = Hatch Distance in mm

T = Layer Thickness in mm

Though this relationship is used to calculate the energy density, it does not include characteristics like powder absorptivity, heat of fusion, laser spot size, bed temperature and other important characteristics. However, the formula can be used to calculate the minimum applied energy necessary to achieve adequate material fusion for the desired material properties. Furthermore, it can be used to maximize the build speed by utilizing the fastest combination of laser power, scan rate and spacing for a machine.[2]

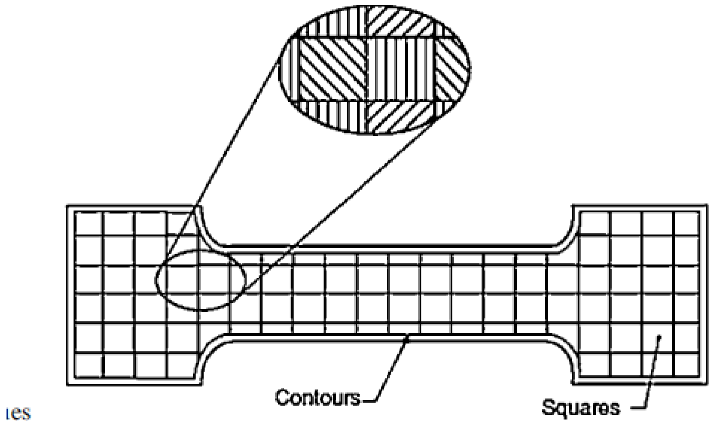

Figure 2.3: Contouring and filling.[2]

2.1.1.2 Scan-related Parameters

Scanning related parameters often directly impacts the formation of residual stresses in the part during the building process. These residual stresses are responsible for part distortion, micro-structural defects and undesirable surface roughness etc. Hence it is important that optimum scan parameters are chosen for a given application. Scanning often occurs in two modes, which is the contour mode and the fill mode as shown in figure 2.3. During contouring, only the outline of the part is scanned. This is done to achieve the highest accuracy and the best surface roughness around the perimeter of the part. The rest of the cross section is scanned using a fill pattern[2].

One of the most common fill pattern is the raster pattern where the laser scans in a back and forth fashion. In some cases the fill section is divided into strips where each strip is scanned sequentially and the strip angle is rotated every layer. Figure 2.4 illustrates different scanning strategies and paths. When it comes to research of scanning strategies with respect to the residual stresses, there are many publications which have interesting results. However, during the literature study it was observed that there are some contradicting results. For instance it was found that Island scanning results in a reduction in residual stresses and using shorter scan vectors reduced the residual stresses. However, according to Kruth et al.[5] and Mercelis et al.[6] island size has no effect on the residual stresses.

Similar to laser parameters, there are some important scan related parameters that determine the formation of residual stresses in the part. The parameters are discussed below:

- **Hatch Offset:** It is the distance between the outermost border and the hatching area.
- **Hatch Distance:** The distance between two neighboring hatch vectors of the fill pattern
- **Hatch Rotation Angle:** Hatch patterns can be rotated by any degree. Generally, two rotation angles are possible. The first value (starting angle) that can be entered is the initial rotation of the pattern; whereas the second value (angle increment) can be used if the pattern is supposed to be incrementally

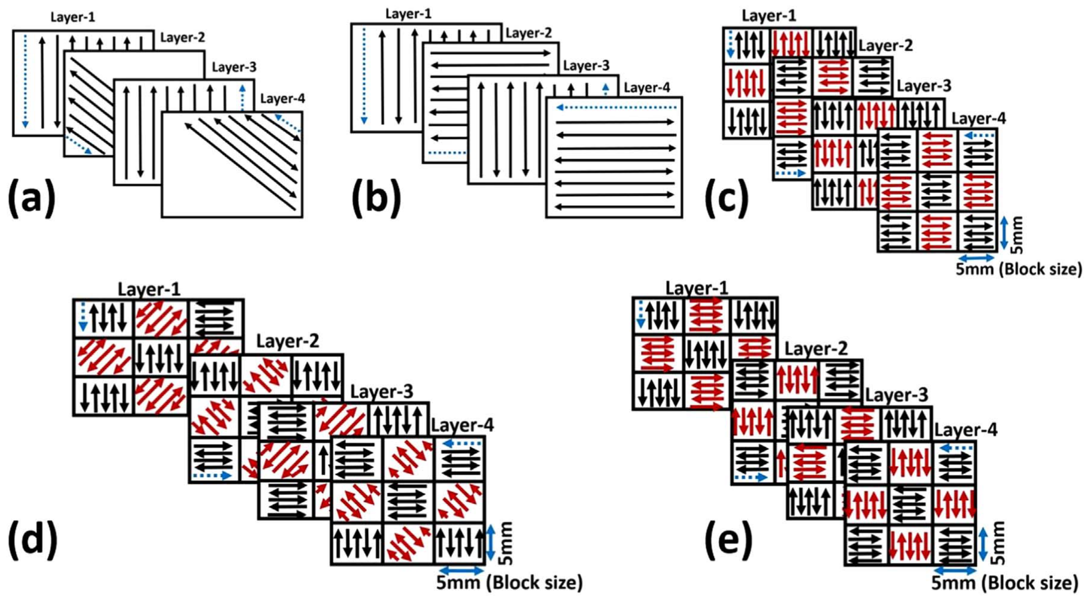

Figure 2.4: Schematics of scanning strategies (a) 45° alternating (b) 90° alternating (c) Schematic of chessboard scanning (d) Chessboard scanning with adjacent chessboard block scanned in 45° rotated direction. (e) Chessboard scanning with adjacent chessboard block scanned in 90° rotated direction.[4]

rotated about a certain angle each layer.

- **Scan Vector Length:** The length defines the width of the pattern element.
- **Scanning Pattern:** There are mainly two types of scanning patterns. Stripe pattern and the chess pattern are the two most commonly used patterns.

2.1.1.3 Powder-related Parameters

Powder shape, size and distribution are some of the main parameters that influence the laser absorption characteristics as well as powder bed density. Finer particles provide greater surface area and absorb laser energy more efficiently than coarser particles. Powder bed temperature, laser power, scan speed and scan spacing must be optimized in order to achieve the best possible part geometry and surface roughness. The powder bed temperature should be kept uniform and constant to achieve repeatable results. Generally, high-laser-power/high-bed-temperature combination produces dense parts, but can result in part growth, poor re-cyclability, and difficulty cleaning parts. On the other hand, low-laser-power/low bed-temperature combination produces better dimensional accuracy but result in lower density parts and a higher tendency for layer de-lamination. High laser power combined with low part bed temperatures result in an increased tendency for nonuniform shrinkage and the build-up of residual stresses, leading to curling of parts. The powder bed density, as governed by powder shape, size, distribution, and spreading mechanism, can strongly influence the part quality. Powder bed densities typically range between 50 and 60% for most commercially available powders, but may be as low as 30% for irregular ceramic powders. Generally, the higher the powder packing density, the higher the bed thermal conductivity and the better the part mechanical properties.[1]

2.2 Geometrical Inaccuracies

The difference between the nominal and the actual geometry defines the concept of geometrical inaccuracy. In this section former studies about the level of geometrical accuracy obtained in the L-PBF processes is reviewed and the standard system of GD&T and principals of optical measurement techniques are listed.

2.2.1 Former Studies on Geometrical Deviation of AM Parts

L-PBF is a method of additive manufacturing(AM) which is capable of producing end-use parts directly from CAD data[7]. Manufactured parts by L-PBF are near full density and have mechanical properties comparable to bulk materials[8, 9]. Several defects usually exist in an L-PBF part. High thermal stresses might lead to severe distortion and cracks and the balling effect causes poor surface finish[10]. As a result of locally concentrated energy input, the temperature gradient mechanism(TGM) and the related plasticizing lead to residual stresses and distortions[11, 12] and anisotropic shrinkage which occur in forming the melt pool from condensed powder and then subsequent solidification which leads to volume shrinkage assist this mechanism[13, 14, 15, 16, 17, 18]. Phase transformation in some alloys also might have a notable contribution in induced shrinkage during L-PBF processes and help forming residual stresses which has been studied thoroughly[13, 14, 16, 19, 20]. This large amount of residual stress reduces the part geometrical accuracy and detrimentally influences the functional performance of the end-use parts[21]. To address the aforementioned problems of SLM, extensive research has been conducted to realize the effect of process parameters on residual stresses in printed parts. The results of these studies with different materials, measurement strategies and parameters do not all lead to the same conclusions. The early studies in Laser-PBF[22, 6, 23] show that the largest residual stresses exist perpendicular to the scan direction; while the more recent works state that the greatest residual stress is parallel to the scan vector[24, 34]. Regardless of the direction of principal stress, there is no doubt that the use of unidirectional scan vectors that are aligned layer after layer will give a very an-isotropic state of stress. Several studies have been done to compare the residual stress resultant of different scan strategies[24, 5, 25, 26, 27, 28]. It is proven that shorter scan lines[31, 35, 36, 37] and scan vector reduction[38] yield lower residual stresses. Other researchers argued the potential to minimize residual stresses by altering the scanning orientation[34, 37, 38, 39]. Some studies have concerned the optimum hatch angle to achieve the lowest and most uniform residual stress and better mechanical properties. These studies resulted in finding few specific angles really helpful to distribute the residual stresses more evenly[40]. The use of checkboard or alternating scan strategies are common for distribution and reduction of residual stress[41]. Robinson et al[42] compared the resultant residual stress of unidirectional, bi-directional and checkboard pattern scanning strategies on samples made of pure titanium powder. The use of checkboard scanning strategies was shown to have little benefit in reducing the residual stress but bi-directional scanning (XY alternating strategy) gave the lowest measured and the most uniform distribution of residual stress. In contradiction, Yasa showed that island scanning pattern can result in 40 percent reduction in residual stresses[43] and Kruth et al[23, 30] concluded that checkboard scanning reduces the level of residual stresses significantly but changing the island size does not contribute any further improvement; while Yanjin Lu et al[44] found that by increasing the island size, the residual stresses decreases; but Amanda et al[45]reported an increase in residual stress with larger islands. In some other research cellular[46] and helix[47] scan strategies found to be beneficial to alleviate the level of maximum residual stress induced in printed parts. And Qian Bo[48] studied the feasibility of manufacturing sophisticated features and geometries using raster and helix strategies and revealed that helix strategy is the only one which is applicable to manipulate some geometries like turbine blades. To best knowledge of the writer, no specific research has been done so far to study the effect of contouring step in different scan strategies in L-PBF on geometry inaccuracies and no obvious effort has been done to evaluate the benefit of contouring on surface roughness of printed parts via L-PBF process.

2.2.2 Geometrical Dimensioning and Tolerancing

The standardized system used for defining and communicating engineering tolerances such as shape, size, form, orientation and location of features on a part is called Geometrical Dimensioning and Tolerances(GD&T) which describes the nominal geometry and the allowed tolerances of a part. The geometrical characteristics defined by the American Society of Mechanical Engineering(ASME) are shown in figure 2.5.

2.2.3 Optical 3D Measurement

Non-contact optical three-dimensional measuring, scanning and digitising are increasingly present in quality assurance systems. Simple scanning procedures, high density of data acquired in a single scan, and the possibility of integrated reverse engineering and inspection, are all advantages of optical scanning compared to conventional measuring methods. Due to the three-dimensional acquisition of measuring data, an optical scanner is often considered to be an alternative possibility for coordinate measuring machines. However, the accuracy of the measured data acquired by optical scanning (even with a high-end system) is still far below the level achieved by high-level coordinate measuring machines. A three-dimensional optical scanner acquires geometry data from an existing physical object. This data is used to construct a virtual three-dimensional model of the scanned object that can be used for various applications, such as reverse engineering, inspection and quality management, rapid prototyping, cultural heritage documentation and restoration.

2.3 Surface Roughness

Surface roughness characterizes the surface texture through various parameters. Surface topography is one of the challenges for the development of the metal additive

Tolerance	Geometric Characteristic	Symbol
Form	Flatness	⏥
Form	Straightness	—
Form	Circularity	○
Form	Cylindricity	⌭
Profile	Profile of a line	⌒
Profile	Profile of a surface	⌓
Orientation	Perpendicularity	⊥
Orientation	Angularity	∠
Orientation	Parallelism	//
Location	Symmetry	⌯
Location	Position	⌖
Location	Concentricity	◎
Run-out	Circular run-out	↗
Run-out	Total run-out	⌰

Figure 2.5: GD&T Symbols[49].

manufacturing promising technique and obtaining good surface finish is a very critical issue in many applications to prevent surface-initiated cracking and resultant premature failure[50].

2.3.1 Previous Research on Surface Roughness of AM Parts

SLM still faces an apparent limitation in terms of surface quality if compared to some alternative metal manufacturing processes such as machining. Surface quality is greatly influenced by the "stair step" effect, which is the stepped approximation by layers of curves and inclined surfaces. Poor surface quality could lead to long and expensive post-finishing operations, often executed by hand due to the shape complexity of the parts produced, thus compromising the advantages of using the AM processes for industrial production. Furthermore, a smooth surface is limited by the balling phenomenon that occurs during laser melting[51]. Previous studies have attempted to predict the surface roughness of parts processes on different additive layer manufacturing(ALM) platforms[52, 53, 54, 55, 56]. However, these models based on the pure description of the stair step profile frequently fail to accurately predict the surface roughness of the parts because surface roughness is influenced also by other process parameters[51]. Several studies have investigated the effect of other parameters of SLM including build orientation, laser power, layer thickness, beam speed, hatch spacing and contouring step on surface roughness of the parts[51, 57, 58, 59, 60, 61]. Koutiri et al[57] studied the effect of SLM parameters on surface finish of as-built Inconel 625 parts. They found out the laser power has a two-fold influence on surface roughness; On one hand, higher powers cause layer remelting and provoke a smoothing effect and on the other hand, excessive powers combined with large angles (toward normal vector to the build plate) favor sticking surrounding particles on overhanging parts. In addition, it was revealed that increase in beam diameter causes higher surface roughness. On the contrary, in another research on SLM process it was revealed that down side surface roughness improves by lower laser power while the roughness of up-skin surfaces is unaffected [55]. In the latter research the effect of contouring step on surface roughness was also investigated. The surface finish across all the scan speeds was improved with the help of a contour scan regardless of the layer thickness[60]. To the best knowledge of author, the main focus of former studies has been on investigation of SLM parameters on surface finish rather than scan strategies; so that among the studied articles, the only which addressed this issue is the latter one.

2.3.2 Surface Profile Acquisition Methods

Several techniques are widely used to study the topography of printed parts including Contact stylus, Areal topography measurement, Scanning Electron Microscopy(SEM) and X-ray computed tomography; with their specific applications and drawbacks. Comparing of results achieved via contact stylus with optical measurements has revealed that stylus profiles do not catch correctly the topography; obtained roughness values are constant with increasing inclination whereas optical measurements show a surface degradation with inclination. Several reasons might be proposed as the stylus deteriorates with such surfaces and mechanical filtering due to the tip radius occurs on the bed of partly melted particles[62]. On the other side, areal topography measurement is clearly the growing field for AM surfaces. Different measuring techniques exist in this field but Imaging Confocal microscopy(IC), Focus Variation microscopy(FV) and Coherence Scanning Interferometry(CSI) are the most used techniques and have been compared by Thompson et al.[63, 64].

The acquisition machine used in this project is Sensofar-S-neox installed along with Accurion Halcyonics-i4 active vibration isolation platform allowing dynamical control over external vibration which reduce errors caused by vibrations. The machine allows three modes of acquisition, namely, focus variation microscopy, confocal microscopy and coherence scanning interferometry. The method we used to study the topography of these samples is the combination of both FV and IC techniques which is called Confocal Fusion. This technique provides good results for steep angles alongside providing good lateral resolution.

2.3.2.1 Imaging Confocal

Imaging confocal microscopy is a well-known technology for the 3D measurement of surface topography. A confocal microscope is used for the acquisition of a sequence of confocal images through the depth of focus of the objective. A confocal microscope produces optically sectioned images of the sample under inspection by restricting the illuminated regions on the sample by means of a structured illumination pattern and observing the reflected light by using a pin hole or set of them to block the light that comes from the surface out of focal plane(fig.2.6)[65].

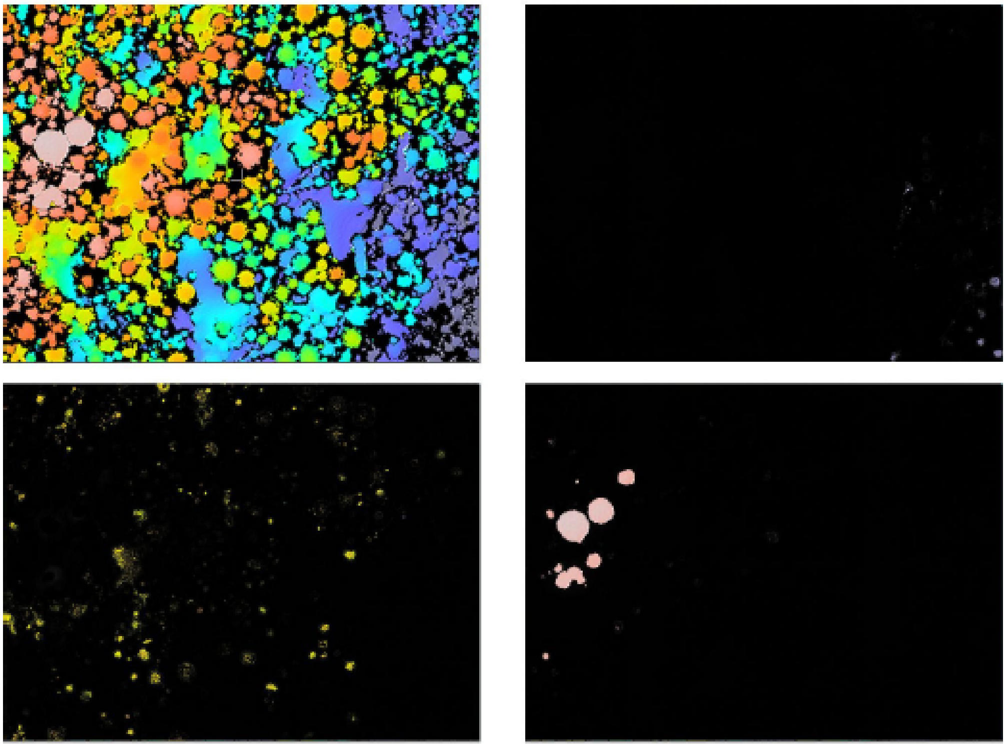

Figure 2.6: Overall surface roughness profile (upper left); Conjugate points with respect to height for the lowest layer (upper right), middle layer (lower left) and highest layer (lower right)[66].

2.3.2.2 Focus Variation

The focus variation method uses vertical scanning with limited depth of focus. Because of its ability to measure steep flanks and its robustness in relation to different materials, focus variation enables the measurement of roughness and form at the same time. Depth measurement by focus variation is performed by searching the best focus position of an optical element pointing to a sample. This focus position is related to a certain distance from the sample (depth) value. By carrying out this process for many lateral positions, a depth map of the sample is generated.

2.3.2.3 Confocal Fusion

As mentioned earlier, Confocal fusion acts as a mixture of both FV and IC techniques. Confocal microscopy can take care of a smooth surface better than focus variation microscopy while focus variation microscopy will help confocal microscopy by providing data from a rough surface. There are three main fusion techniques that are used in confocal fusion: Topographical fusion, Image fusion and Axial response pixel-by-pixel fusion. Image fusion and Axial response use a dynamic algorithm and can yield results with spatial frequencies close to confocal data.

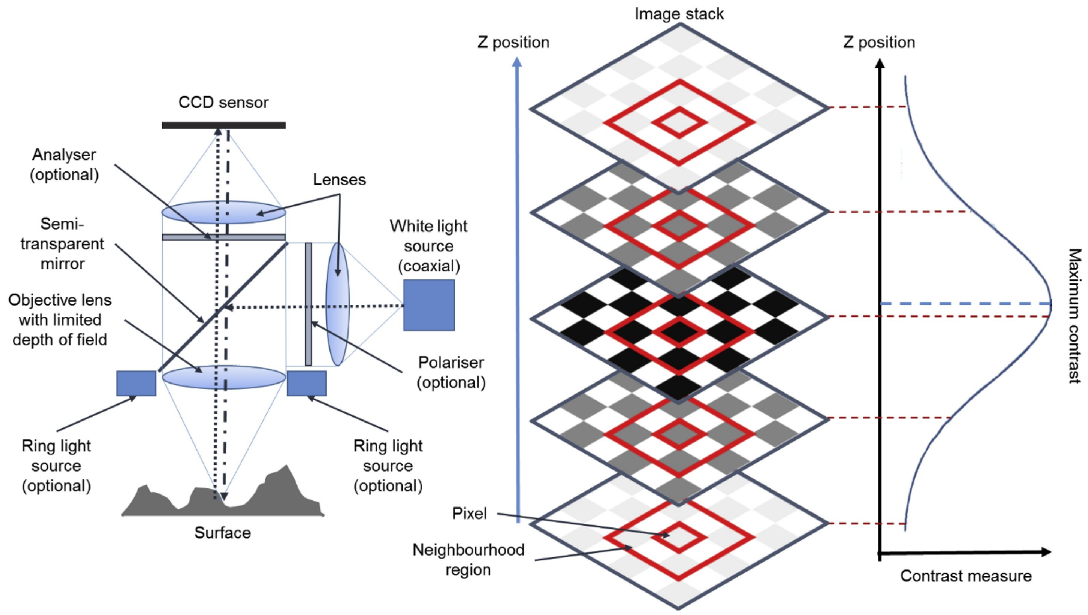

Figure 2.7: Schematic diagram of the focus variation technology; a) elements of the optics system; b) images captured during vertical scanning, arranged as a stackc) the contrast curve associated to the example pixel, obtained by interpolation between contrast values from the image stack.[67].

2.3.3 Surface Profile Analysis

A brief definition of surface parameters which are analysed in this project is given here[68]:

2.3.3.1 Arithmetic Mean Height, Sa

The arithmetic mean height or Sa parameter is defined as the arithmetic mean of the absolute value of the height within the measured area, A.

$$S_a = \frac{1}{A} \int\int_A |z(x,y)| dxdy \tag{2.2}$$

2.3.3.2 Root Mean Square Height, Sq

The root mean square height or Sq parameter is defined as the root mean square value of the surface departures, z(x,y), within the measured area, A. The Sa and Sq are strongly correlated to each other, however the Sq parameter is more reliable in terms of statistical significance(it is standard deviation).

$$S_q = \sqrt{\frac{1}{A} \int\int_A z(x,y) dxdy} \tag{2.3}$$

2.3.3.3 Skewness, Ssk

In statistics, skewness is a measure of the asymmetry of the probability distribution of a real-valued random variable about its mean. The skewness value can be positive or negative, or undefined. Negative skew commonly indicates that the tail is on the left side of the distribution, and positive skew indicates that the tail is on the right. In other words, skewness describes the shape of the topography height distribution. For a surface with a random (or Gaussian) height distribution that has symmetrical topography, the skewness is zero. A symmetrical profile gives an amplitude distribution curve that is symmetrical about the centre line and an unsymmetrical profile results in a skewed curve. Skewness is calculated through below equation:

$$S_{sk} = \frac{1}{{S_q}^3}\frac{1}{A}\int\int_A z^3(x,y)dxdy \tag{2.4}$$

2.3.3.4 Kurtosis, Sku

In probability theory and statistics, kurtosis is a measure of the "tailedness" of the probability distribution of a real-valued random variable. In a similar way to the concept of skewness, kurtosis is a descriptor of the shape of a probability distribution. In other words, kurtosis parameter is a measure of the sharpness of the surface height distribution and is the ratio of the mean of the fourth power of the height values and the fourth power of Sq within the sampling area(A). Kurtosis is strictly positive and unit-less, and characterises the spread of the height distribution. A surface with a gaussian height distribution has a kurtosis value of 3. Unlike Ssk, use of this parameter not only detects whether the profile spikes are evenly distributed but also provides a measure of the spikiness of the area. A spiky surface will have a high kurtosis value and a bumpy surface will have a low kurtosis value.
The Ssk and Sku parameters can be less mathematically stable than other parameters since they use high order powers in their equations, leading to faster error propagation.

$$S_{ku} = \frac{1}{{S_q}^4}\frac{1}{A}\int\int_A z^4(x,y)dxdy \tag{2.5}$$

2.4 Simulation of L-PBF Process

With the use of CAE and FEA tools, designers are aggressively reducing their product's time-to-market, cost, and material consumption. Many researchers have already proposed different ways to simulate powder bed fusion processes. A few of them[69, 70] have created 3D finite element (FE) models for the temperature evolution during laser sintering and some researchers[71] have proposed a FE method for calculating the temperature and stress distribution in a single layer of sintered material. Parallel to extensive academic effort to simulate these type of AM processes, few acceptable progress have been made in development of commercial tools. The authors know few simulation tools for metal additive manufacturing processes; Including SemuFact, Ansys-Additive and Comsol multiphysics. Based on the best knowledge of authors, although these softwares have simulated many asects of the process successfully, but they are not yet mature enough to accurately simulate the process due to necessary simplification which is taken in solving problems. Due to simplicity and being user friendly, in this thesis, Ansys-Additive software was used to simulate the SLM of preliminary designed artifacts to investigate the effect of various parameters on distortion and residual stresses in different features. finally this tools was used to simulate the SLM process on the final artifacts as well.

2.4.1 Simulation Types

There are three types of simulations available in this software; Assumed Strain Simulation, Scan Pattern Simulation, and Thermal Strain Simulation.

2.4.1.1 Assumed Strain-Isotropic

Assumed strain mode is the fastest simulation type available. It assumes that a constant, isotropic strain occurs at every location within a part as it is being built. The strain is determined by this equation:

$$strain = SSF * \frac{\sigma_{yield}}{E} \tag{2.6}$$

The Strain Scaling Factor (SSF) must be experimentally retrieved for each set of machine/material/strain/stress mode combination of interest.

2.4.1.2 Scan Pattern Strain-Anisotropic

This strain mode uses the same average strain magnitude as assumed uniform strain, but it subdivides that strain into anisotropic components based on the local orientation of scan vectors within the part using anisotropic factors which should be calibrated for each set of machine/material/stress/strain mode. This strain mode requires the creation of scan vectors using user-provided scan settings or by reading scan vectors from a machine's build file (In this project "Magics Materialise" was used).

2.4.1.3 Thermal Strain-Anisotropic

This strain mode provides the highest degree of accuracy by predicting how thermal cycling affects strain accumulation at each location within a part. A "thermal ratcheting" algorithm assigns a base strain to each location within the part as it solidifies. Each time a location within the part is heated above a temperature threshold (approximately 40% of its absolute melting temperature); an increase in strain in that location occurs. If a location remelts, the strain is reset to the base strain. The more times a location is heated above the threshold without melting, the higher the strain accumulates. Once the strain magnitude is calculated for each location within a part using the thermal ratcheting algorithm, that strain is passed to the Mechanics Solver and applied as an anisotropic strain based upon both local strain magnitude and local scan orientation. Because thermal strain requires a thermal prediction for every scan vector, this strain mode requires a much longer computational time. As in assumed strain and scan pattern simulations, we should do calibration for strain scaling factor.

2.4.2 Voxels

A voxel is a hexahedral (cubic) element used in the finite element method. In the following figure of a cubic part, a voxel is shown in red. There are eight voxels in the cube. Voxel size is the length of the yellow line.

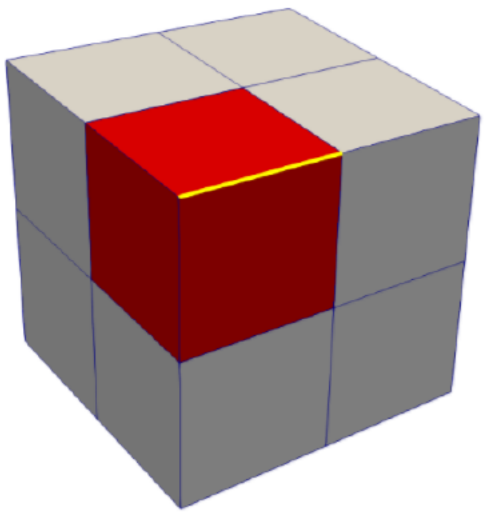

Figure 2.8: Voxels in Ansys-Additive[72]

The voxelization function divides the part domain into voxels for simulation in the mechanics solver. The technique employs subvoxels within each voxel to better represent geometry, in particular at edges and curves. For clarification, see figure 2.9 where a voxel sample rate of 5 has been used. Any subvoxel which the geometry passes through is counted. In this specific example, 70 out of 125 subvoxels are counted; so the voxel density is 70/125=56%. Then material properties in this domain is scaled down by 56%.

2.4.3 Elastoplastic Model

Once you choose a material, you have to choose material behavior in calculations of stress that is either linear elastic or elastoplastic. The elastoplastic calculations are based upon the J2 (von Mises) plasticity model. To provide further information about the material's behavior in the plastic deformation region, the strain hardening factor(μ) is used to calculate the slope of the stress-strain curve beyond the material's yield stress(E_p) (see figure 2.10).

$$E_p = E * \frac{\mu}{1 - \mu} \tag{2.7}$$

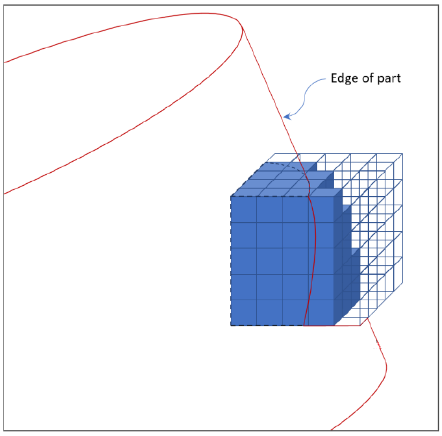

Figure 2.9: A geometry domain passing through a voxel which consists of 125 subvoxels[72].

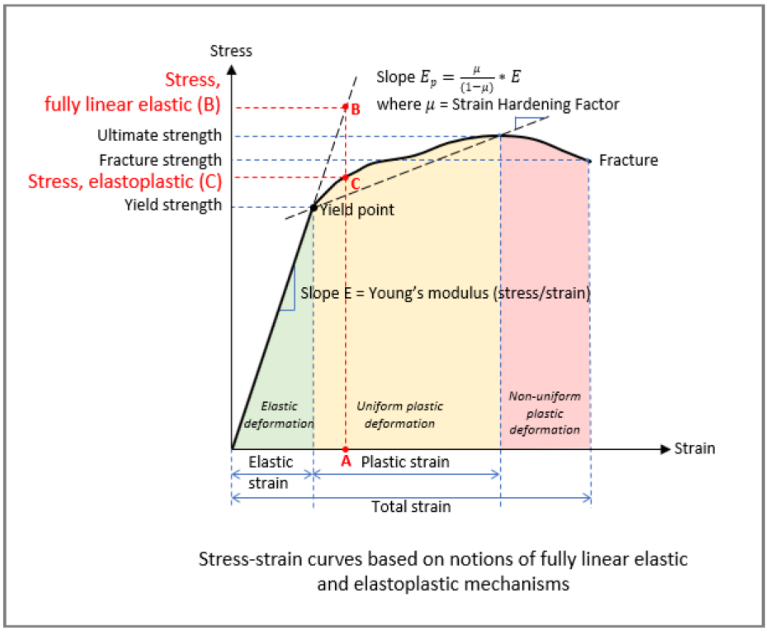

Figure 2.10: Relation between the slope of stress-strain curve in plastic zone(E_p) and strain hardening factor(μ)[72].

3

Methods

This section cover the methods and processes that were used to conduct the research project on.
Below is a schematic diagram of the research approach used in this project.

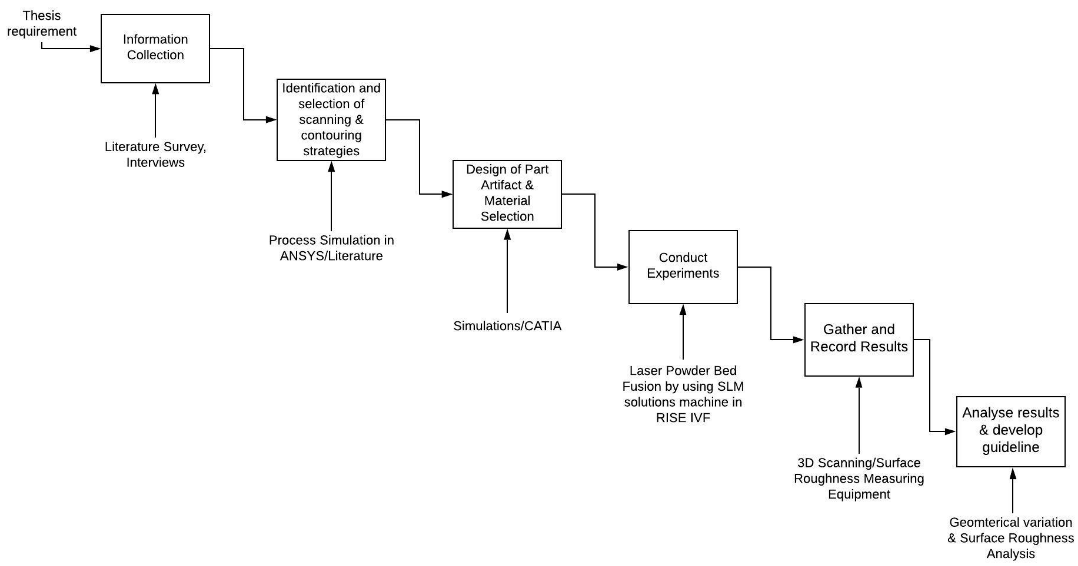

Figure 3.1: Schematic diagram of the research approach used in this thesis.

The steps are explained in detailed below:

- The initial step is to gather and collect information using literature survey and conducting interviews with the industry experts.
- The information from the above step was analyzed and the scanning and contouring strategies were selected for the experiments.
- The design of the part artifact was done using CATIA.
- As soon as the part artifact's design is done, the part was printed in RISE IVF using the SLM solutions machine.
- The printed parts were 3D scanned to perform the geometrical variance analysis. The parts were also used to conduct the surface roughness measurements. The results from these analyses are gathered and recorded.
- The results were analyzed and compared with respect to various factors. The results were recorded and documented in the final thesis report.

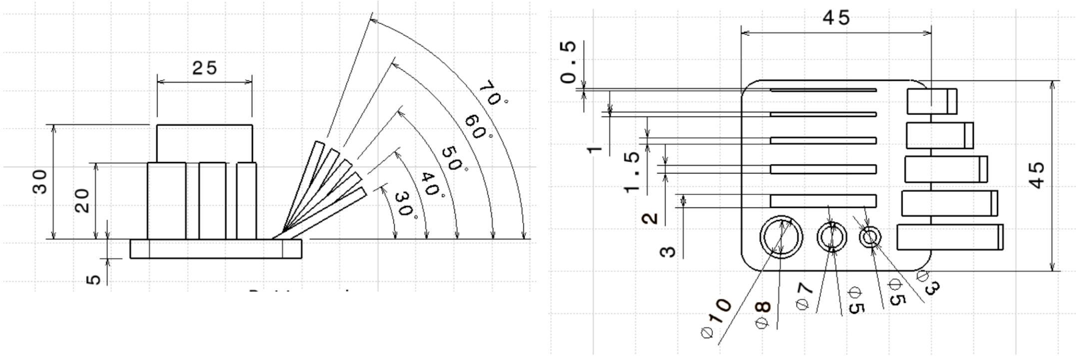

Figure 3.2: Left:Front view and Right: Top view of Primary artifact for preliminary simulations(dimensions in mm).

3.1 Information Collection

3.1.1 Literature Review

One of the main methods to acquire knowledge and information is to read through various literature about the research conducted on similar topics as this thesis. Initially, literature about various process parameters that are involved in selective laser melting was studied. Subsequently, the study was narrowed down to the parameters that are directly related to the scanning strategies like, hatch angle rotation, scan vector length, hatch distance, hatch offset & scanning path. Finally, a study was carried out on the materials for which the above-mentioned parameters are being optimized for, like Ti6Al4V, AlSi10Mg & SS316L.

3.1.2 Interviews

It was important to get industry insights as to how scanning strategies play a role in optimizing process parameters for a particular material in L-PBF. Therefore, an interview was conducted with a company called Lasertech which is situated in Karlskoga, Sweden. This company specializes in industrial metal additive manufacturing. Adding to that, an interview was conducted with Christophe Lyphout who is a researcher in additive manufacturing at RISE IVF. It was decided that some insights from the academic side was important to gather. Therefore, we conducted a rather brief discussion with Eduard Hyrha who is the head of CAM2 at Chalmers.

3.2 Identification & Selection of Scanning Strategies

From the literature review and the interviews, it was decided to conduct some preliminary process simulations in ANSYS-Additive to understand the behaviour of various scanning parameters. A sample part artifact was design in CATIA with important geometrical features like thick walls, thin walls, cylinders and overhangs(figure 3.2).

3.2.1 Simulation by Ansys-Additive

The simulation process consists of four steps: finding the proper simulation settings, set up the scan strategies, adjusting material specifications and review the results.

3.2.2 Simulation Settings

To investigate probable effective parameters on the distortion of parts, a set of simulations on the primary test artifact was conducted. The artifact includes walls with different thicknesses, inclined bars with 5 different angles and three hollow cylinders in three sizes (see fig.3.2). In these simulations, effects and capabilities of this software was explored in order to be considered as the optimum options for the final runs on the main artifact. These parameters are simulation type, voxel to layer thickness ratio and the ability of Ansys-Additive to distinguish various scan patterns.

3.2.2.1 Simulation Type

Since the thermal strain mode of simulation was extremely time consuming, the scan pattern strain simulation was chosen. All the anisotropic coefficients and strain scaling factors were kept the same as the default values, because conducting calibration runs in printer was not possible in that time of project.

3.2.2.2 Voxel Size

To investigate the effect of voxel size, a small slant cube (see annex for geometric dimensions and simulation results) was simulated by four different voxel size (30, 90, 150 and 240 μm corresponding to 1,3,5 and 8 times of layer thickness). The size of the cube was chosen very small so that the simulation of the smallest voxel size could be executable.

3.2.2.3 Scanning Patterns

According to the latest version of Ansys-Additive manual, this tool cannot simulate contouring and border scans. On the other hand, the capability of this tool to distinguish between different laser beam vector lengths or to differentiate between various scanning patterns (different rotation angles) was doubtful. Therefore, one simulation was done with default stripe pattern, which means 33° rotation angle in consecutive layers and a vector length of 10 mm, two simulations with smaller vectors and one with a vector length of 10 mm and rotation angle of 67° (table 3.1). Based on the maximum residual stresses and deviations in the components and the place where these maximum values are observed (see annex 1); it was realized that this software takes the different rotation angles into consideration but cannot distinguish between various vector lengths.

Table 3.1: Maximum residual stress and distortion recorded in the artifact with four strategies with stripe scanning pattern.

Rot.degree,Vector Length	33,10mm	33,2.4mm	33,5mm	67,10mm
Residual Stress(MPa)	1315.2	1315.2	1315.2	1322.5
Max Distortion(mm)	0.138	0.138	0.138	0.107

3.2.3 Scanning Strategies Set up

The artifacts are designed in CATIA V5 and then the *.stl file is imported to Magics materialize software to impose desired scanning strategies. The manipulated build file then was used in ansys-additive to allocate material properties and other simulation parameters which were mentioned earlier.

3.2.4 Materials Properties Set up

There are several parameters which should be justified by introducing a new material in the library of Ansys-Additive. Powder absorptivity and Solid absorptivity were taken similar to 17-7PH stainless steel due to the lack of accurate coefficients for this material. In addition, anisotropic strain coefficients were taken 1.5, 0.5 along and perpendicular to the laser beam scanning direction while this coefficient along the z-axis and SSF were kept 1; all as the default values in this software. Strain hardening factor also was calculated according to yield and Ultimate tensile stresses of this material derived from [73](see annex) listed in table 3.2.

Table 3.2: H13 properties and settings for simulation by Ansys-Additive[73]

H13 Properties	**Value**
Powder Absorptivity(%)	57
Solid Absorptivity(%)	40
Thermal Expansion Coefficient(1/K)	0.0000126
Elastic Modulus(GPa)	203
Poisson Rate	0.285
Material Yield Strength(MPa)	1000
Hardening Factor	0.016
Strain Scaling Factor(SSF)	1
Anisotropic Strain Coefficient(||)	1.5
Anisotropic Strain Coefficient(V)	0.5
An-isotropic Strain Coefficient(Z)	1.0

3.2.5 Results Extraction

ParaView version 5.6.0 was used to derive and compare the results of simulations. It is an open-source, multi-platform scientific data analysis and visualization tool that enables us to analyse and visualize extremely large data-sets.

3.2.6 Final Simulations

After evaluation, the final part artifact was designed by finding the probable effective parameters on deviations of a sample(Fig.2). Three distinct simulations with different hatch rotation angles were run under "Thermal Strain" simulation type which is the most accurate solver. The main difference between these patterns is the rotation angle between consecutive layers (180°, 67° and 10°). The first one corresponds to printed samples named "D", the 10° rotation angle corresponds to "F" and 67° rotation mimics the strategy taken to print artifacts with "E" labels. As it was mentioned, this software cannot simulate contouring steps and hence, running the strategies with contouring steps (A,B,C) was not possible. In table 3.3, selected simulation parameters are listed.

Table 3.3: Parameters for simulations on final artifacts.

Material	H13 tool steel
Voxel size(mm)	0.5
SSF	1
Anisotropic strain coefficients	Default
Hardening coefficient	0.016
Support included in Simulation	No

3.3 Design & Material Selection of Part Artifact

A part artifact is used to test the effect of varying the parameters on the geometry. The design of the part and the material is discussed in this section.

3.3.1 Design

The design of the part artifact was finalized by observing the trends in the simulation. Due to the size constraints in the machine, it was decided to choose the most vulnerable features in the part based on the primary simulations and use those features for research. Therefore, considering the simulation results and inputs from application engineers, the below part artifact was the final model that was printed for different scanning strategies that were planned.

There are three main features in this part artifact that is intended to be investigated:

1. **Walls:** The thickest wall which is 3 mm thick and the thinnest wall which is 0.5 mm thick were chosen from the preliminary part artifact.

2. **Overhangs:** 45 degrees and 15 degrees overhangs were chosen from the preliminary part artifact.

3. **Half-Cylinder:** An inside radius of 2 mm and outside radius of 4 mm were selected.

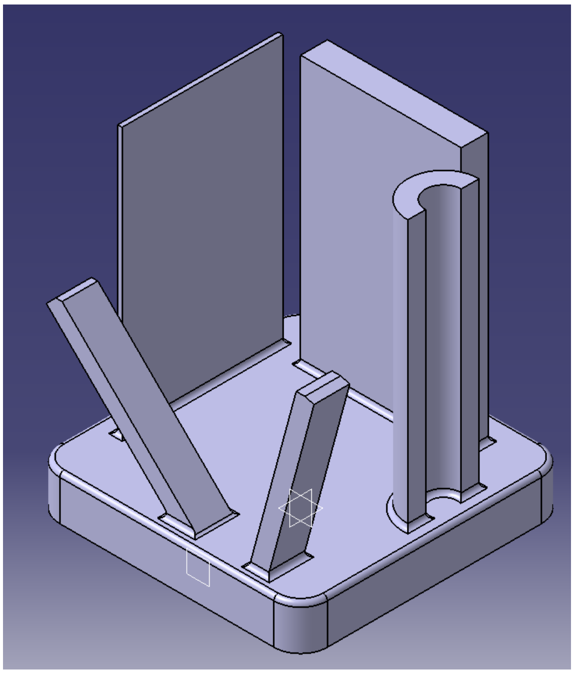

Figure 3.3: Isometric view of the part artifact.

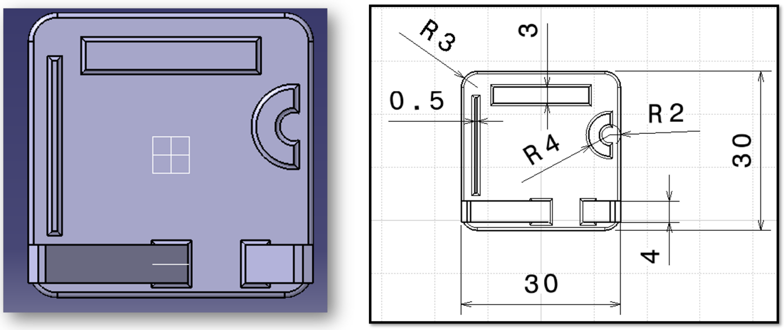

Figure 3.4: Top view of the part artifact(dimensions in mm).

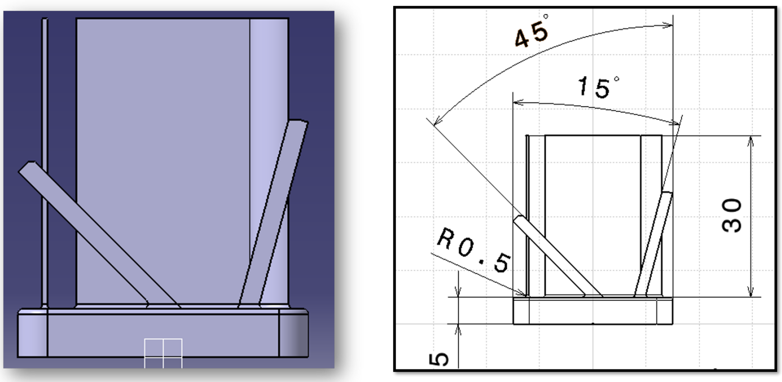

Figure 3.5: Front view of the part artifact(dimensions in mm).

3.3.2 Material

The material that was chosen to conduct the experiments is H13 tool steel. The material properties can be accessed in the appendix. This material was chosen based on the degree of complexity of printing in L-PBF and also because there is not much literature on H13 tool steel. Hence, it was decided to be used in this research. H13 tool steel is also a very suitable material for additive manufacturing applications in the automotive sector as it is one of the most commonly used materials to produce hot-working tool inserts.

3.4 Printer Settings and L-PBF Parameters

The parameter that was chosen from the simulations and the literature is the hatch angle rotation. It was decided to print two parts for each strategy in order to check for consistency between results. The table 3.4 shows the chosen rotation angles.

Table 3.4: The scanning strategy used for printing the parts.

With Contouring			Without Contouring	
Label Name	First angle-Rotation angle		Label Name	First angle-Rotation angle
A	0-180		D	0-180
B	57-67		E	57-67
C	0-10		F	0-10

The other parameters like laser power, scan speed, layer thickness, and spot diameter were kept constant. These parameters were already in use by RISE for printing parts in H13 tool steel.

3.5 Measurement Strategy

3.5.1 3D Scanning Strategy

Mobile ATOS III Triple Scan is used to acquire the point cloud of component to study the geometrical deviations. Precise fringe patterns are projected onto the surface of the object and are recorded by two cameras. As the beam reaches both cameras and the calibrated projector, surface points are calculated which are intersections of three different rays(Fig.3.6). This automatic principle offers advantages in measuring reflective surfaces and objects with deep indentations. ATOS Triple Scan system sensors use narrow-band blue light to filter out interfering ambient light; therefore, short measuring times can be achieved[74].

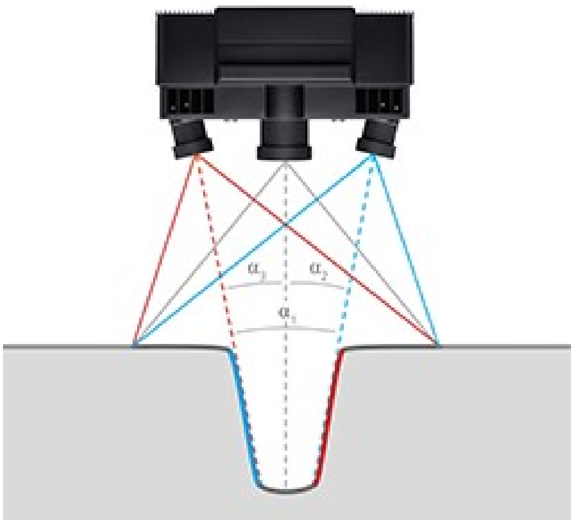

Figure 3.6: The working mechanism of ATOS III Scanner[74].

In this project the printed parts are scanned twice; once before cut-off and the second time after cutting them from the build plate. Before putting the samples, the scanner should be calibrated. In scanning before cut-off, reference stickers are adhered to the surface of the build plate and in several points on the components in various locations for referencing and positioning. For scanning after cut-off samples, the reference stickers are adhered to the surface of components and rotating plate of scanner. Scanning camera is set at certain measuring distance and measuring angle in order to cover the whole measurement volume. The measuring angle is highly dependent on the model's shape but most builds are scanned using the angles 90°, 45° and 30°. The build is scanned at 30° angle right at the center point of the rotating table. Depending on visibility of the build from different angles, the number of division in one rotation is specified equal to 30 degree in the program ATOS Professional to ensure no hindering view. The scanning process has no problem performing under ambient light environment due to the use of 'Blue light technology' which filters out the extra reflecting light that is not the blue light emitted by the scanner. After the build has been scanned from all the angles, ATOS Professional software stitches the data mesh into one file (called point cloud) that will be used for mesh construction and evaluations.

3.5.2 Geometry Evaluation

GOM Inspect 2018 software is used to calculate 3D meshes of scanned components from point clouds, surface reconstruction and nominal-actual comparisons. This software includes all standard alignment functions including RPS alignment, hierarchical alignment based on geometric elements, alignment by reference points and various best-fit methods. This software also makes us capable of doing GD&T analysis; for instance, angularity, planarity and cylindricity of features were measured by this in this project.

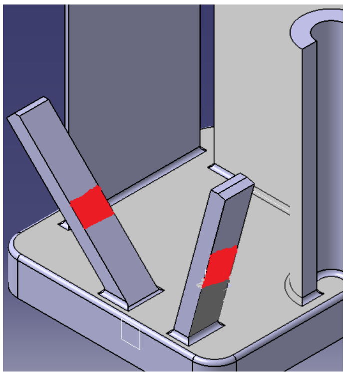

Figure 3.7: precinct of measured area to conduct surface roughness measurements.

3.5.3 Surface Roughness Measurement

After 3D scanning, the inclined bars are cut from the samples by hack saw(it is faster and don't cause the rusting problem occured in EDM cutting again). Then the surface roughness of inclined bars on upside and downside faces are measured with Sensofar S Neox machine which is placed on Accurion Halcyonics_i4 active vibration isolation platform. Aligning of the samples is done roughly by hand and the overview picture is taken with 5x magnification lens. The surface roughness data is obtained with 20x magnification lens through the mean of confocal fusion mode which correlates the data from focus variation microscopy and confocal microscopy. The measurement area is 2.30 mm x 1.65 mm with the resolution of 0.645 μm/pixel. The measurement area is located roughly in the red area shown in figure 3.7. The surface profile obtained by the microscope is analysed by "Mountains Map Premium 7.4" surface analysis software. Since we have a certain amount of Non-Measured Points (NMP) in each profile(beige-colored zones in upper picture in 3.8), this program can interpolate mesh points and it is also capable of flat surface leveling and surface form removing. Calculations of all parameters are based on ISO 25178 standard. By "MountainsMap" software and according to the algorithm shown in figure 3.8 the noise and form of the surface were filtered. Then the leveled surface was used to calculate the surface parameters(lower picture in 3.8). In total 48 accepted measurements were made; 24 on 15° inclined bars and 24 measurements on 45° ones.

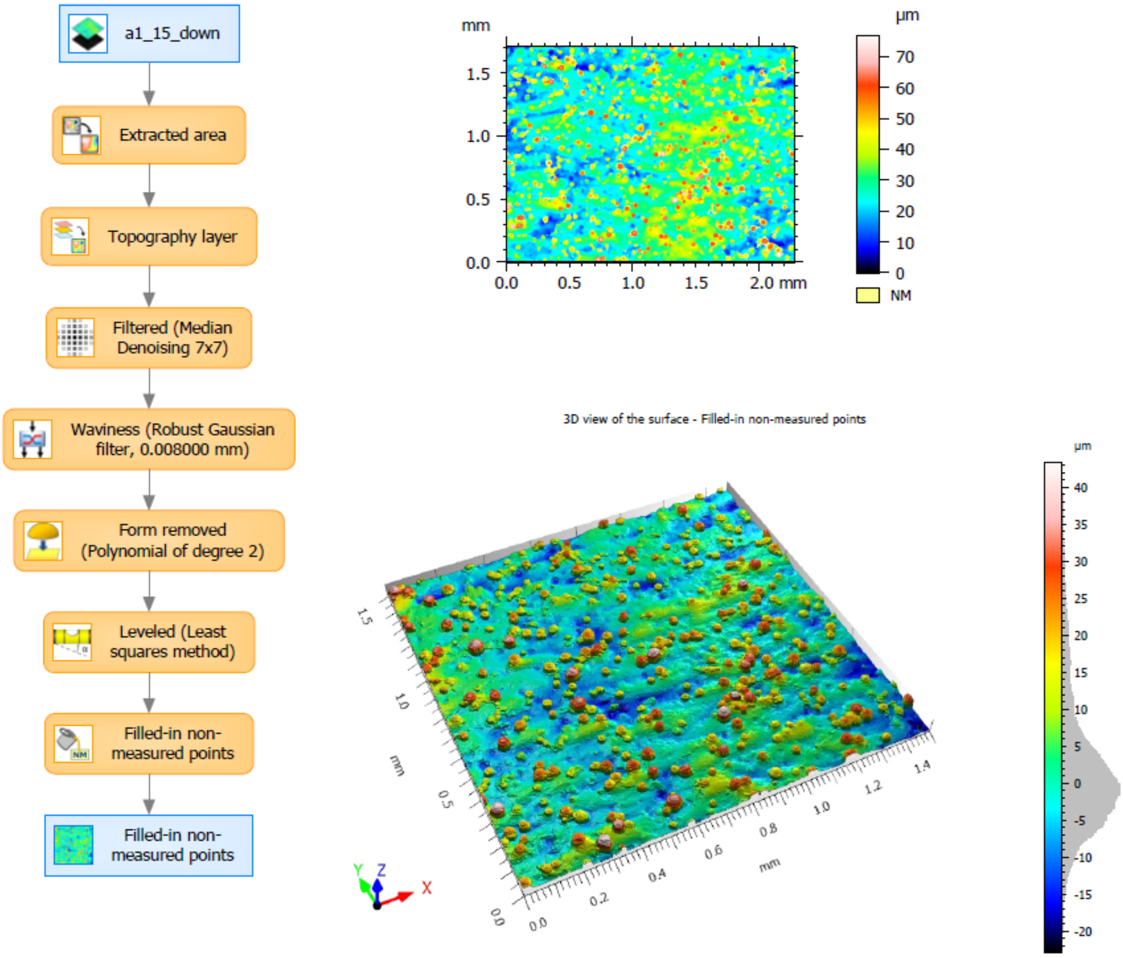

Figure 3.8: Algorithm used in "MountainsMap" software to filter noise and form from scanned areas of samples.

4

Results

This section presents the results from simulations executed by Ansys-Additive. Followed by with the results of geometrical deviation of artifacts measured by 3D-scanner both before and after cut-off from build plate are shown. Finally, surface roughness measurements of inclined bars by Sensofar S-Neox optical profilometer are presented.

4.1 Simulation Results

The results of simulations run with different voxel sizes and the level of residual stresses in primary and final artifacts are depicted here.

4.1.1 Primary Simulations

4.1.1.1 Voxel Size Effect

Except the smallest voxel size which is equal to layer thickness (30 micron), simulation with voxels with other sizes gave us almost the same results in the slant cube(fig.4.1). Therefore, In the main simulation we used the suggested voxel size (500 micron) to have a simulation with reasonable cost.

4.1.1.2 Different Scanning Strategies

Several preliminary simulations were done on the primary artifact for two main reasons: To study the effect of different scanning strategies and to find out the best

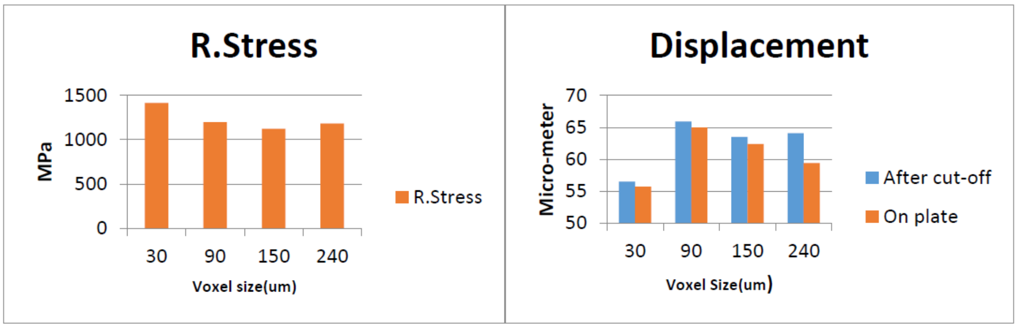

Figure 4.1: Maximum residual stress and displacement in slant cube with various voxel sizes.

simulations.png

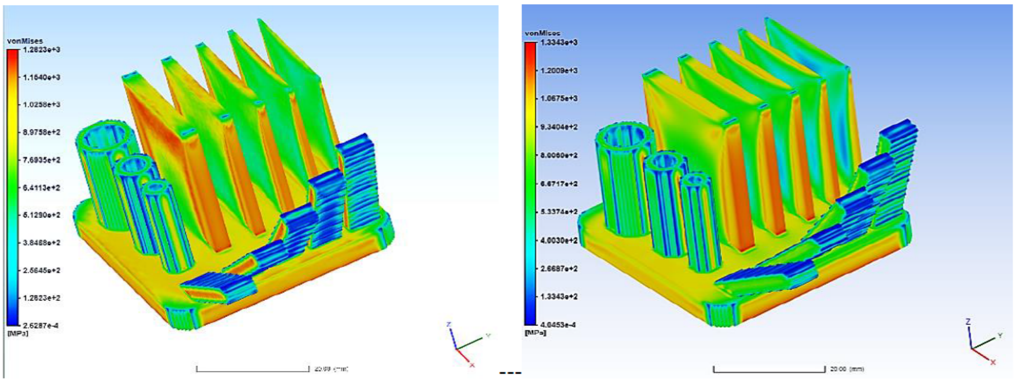

Figure 4.2: Anticipated residual stress in primary artifact by Ansys-Additive: Default chess scanning strategy(left), All-X raster scanning strategy(right).

and useful feature to keep in the final artifact. Chess-pattern and Raster scanning strategies with various laser beam vector length and different Hatch rotation angles were run on the primary artifact. In figure 4.2 the state of residual stress in the component while it's still on build plate for two scanning pattern are shown. These simulations helped us to find the most attractive features which should be kept in the final artifact. As it can be seen in fig.4.2, the highest level of residual stresses are seen in thick wall, the largest cylinder and the most inclined bar. Therefore, the thick wall and large cylinder were kept. However, we just kept the 15 and 45 degree, because printing with larger degrees needs support structures.

4.1.2 Final Simulations

The deviation of three selected adjacent points with the coordinates listed in table 4.1, are extracted from the simulation output file. Then the average of deviations in X, Y, Z directions and the resultant amount is calculated for before and after cut-off separately. The average deviations along x,y,z axis and the resultant deviation(Shown as magnitude) are listed In tables 4.2 and 4.3 according to the hatch rotation angle strategies(see table 3.4).

Table 4.1: The coordinates of selected points on thin and thick wall. in output files of simulations

Geometry	X(mm)	Y(mm)	Z(mm)
	-8.5	-12.5	24.5
Thin Wall	-9.0	-12.5	25.0
	-8.0	-12.5	25.0
	-12.0	-8.0	33.0
Thick Wall	-12.0	-7.0	33.0
	-12.0	-7.5	32.5

Table 4.2: Before cut-off averaged deviation.

	Thin wall				Thick wall			
	dX	dY	dZ	Magnitude	dX	dY	dZ	Magnitude
D	0.053	0.002	0.047	0.071	0.015	0.017	0.016	0.028
E	0.042	0.003	0.035	0.055	0.011	0.037	0.023	0.045
F	0.043	0.005	0.035	0.056	0.012	0.038	0.023	0.046

Table 4.3: After cut-off averaged deviation.

	Thin wall				Thick wall			
	dX	dY	dZ	Magnitude	dX	dY	dZ	Magnitude
D	0.000	0.069	0.047	0.084	0.140	0.031	0.004	0.143
E	0.003	0.128	0.052	0.138	0.117	0.064	0.014	0.134
F	0.016	0.126	0.053	0.138	0.123	0.072	0.017	0.144

4.2 Geometry Deviations

The parts were printed in H13 tool steel in RISE IVF and were then 3D scanned to measure the geometry deviations compared to CAD file. The scan was done in two steps, one before cutting the parts from the build plate and then another scan after cutting the parts from the build plate. This is done to measure the change in geometry after the stress has been relieved from the parts.

4.2.1 Data Collection

The data were collected for all the 12 samples and recorded in a similar fashion. In table 4.4 and 4.5 the data collected for A1 sample are listed. The data for other samples can be found in the appendix.

Table 4.4: Typical statistical overview for A1-before cut Off.

Feature	Element	Nominal			Actual			Deviation			
Coordinates		X	Y	Z	X	Y	Z	dX	dY	dZ	dN
Thick wall	Point 6	-12	-7.5	32.5	-11.829	-9.025	32.206	0.171	-1.525	-0.294	1.562
	Point 5	-12	-7	33	-11.364	-6.991	34.973	0.636	0.009	1.973	2.073
	Point 4	-12	-8	33	-11.533	-9.036	33.022	0.467	-1.036	0.022	1.137
Average deviations								**0.425**	**-0.851**	**0.567**	**1.591**
Thin wall	Point 3	-8	-12.5	25	-8.084	-12.553	24.993	-0.084	-0.053	-0.007	0.100
	Point 2	-9	-12.5	25	-8.999	-12.556	25	0.001	-0.056	0.000	0.056
	Point 1	-8.5	-12.5	24.5	-8.499	-12.56	24.498	0.001	-0.060	-0.002	0.060
Average deviations								**-0.027**	**-0.056**	**-0.003**	**0.072**

Table 4.5: Typical statistical overview for A1-after cut Off.

Feature	Element	Nominal			Actual			Deviation			
Coordinates		**X**	**Y**	**Z**	**X**	**Y**	**Z**	**dX**	**dY**	**dZ**	**dN**
Thick wall	Point 6	-12	-7.5	32.5	-11.631	-9.05	32.779	0.369	-1.550	0.279	1.618
	Point 5	-12	-7	33	-11.625	-9.04	33.103	0.375	-2.040	0.103	2.077
	Point 4	-12	-8	33	-11.643	-9.041	33.146	0.357	-1.041	0.146	1.110
Average deviations								**0.367**	**-1.544**	**0.176**	**1.601**
Thin wall	Point 3	-8	-12.5	25	-8.016	-11.929	24.987	-0.016	0.571	-0.013	0.571
	Point 2	-9	-12.5	25	-8.993	-11.933	25.01	0.007	0.567	0.010	0.567
	Point 1	-8.5	-12.5	24.5	-8.516	-11.932	24.507	-0.016	0.568	0.007	0.568
Average deviations								**-0.008**	**0.569**	**0.001**	**0.569**

4.2.2 Observations from Data Analysis

The data from the above tables were analyzed for different scenarios. Four main observations were found as follows:

4.2.2.1 Thin wall of 0.5mm thick could not be printed without contouring.

Figures 4.3 show that thin walls did not reach the desired height and there are visually lots of defects on the walls.

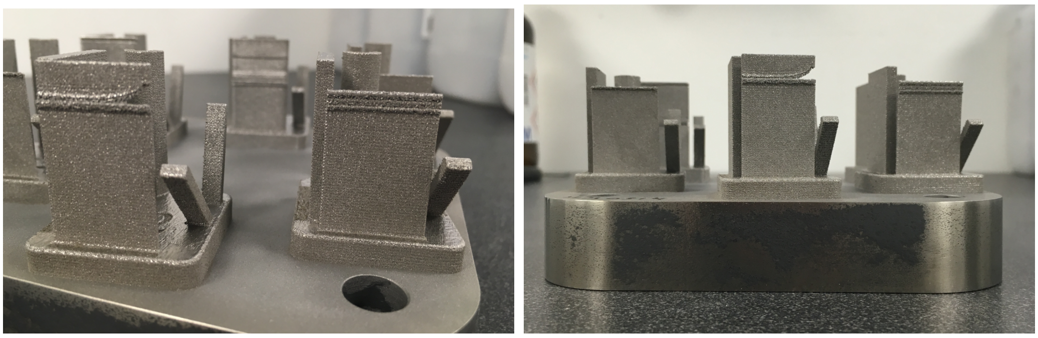

Figure 4.3: Thin walls without contouring.

4.2.2.2 Strategy C: The best for thin wall of 0.5mm-with contouring.

Below is a graph comparing the X,Y,Z deflections for different strategies, before and after cut-off. By considering the deviations of samples after cut-off, which are measured compared to CAD file, it is observed that strategy C has the lowest deviation in all direction that is X,Y and Z. Therefore, it can be concluded that Strategy C which has a 10 degree incremental rotation angle, yields the best results after cut-off for thin walls among contouring strategies.

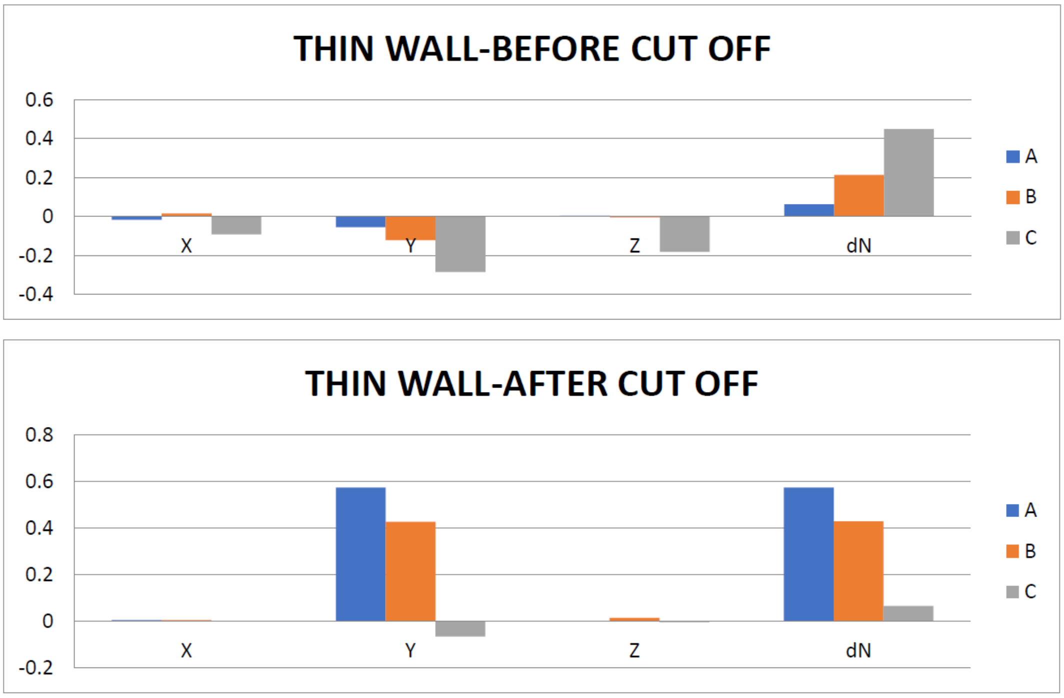

Figure 4.4: Comparison of strategies within contouring thin wall, before & after cut off.

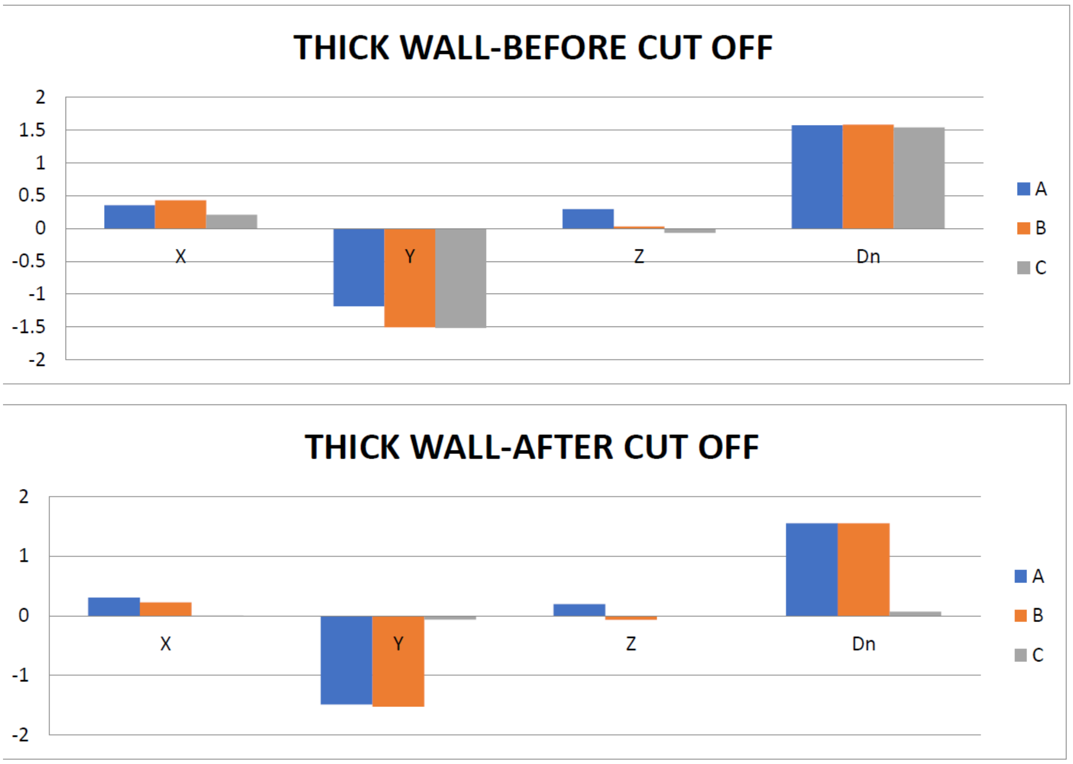

Figure 4.5: Comparison of strategies within contouring thick wall, before & after cut off.

4.2.2.3 Strategy C: The best for thick walls-with contouring.

In figure 4.5 it is seen that strategy C has the lowest deviation in all direction that is toward X and Z. Therefore, it can be concluded that Strategy C which has a 10 degree incremental rotation angle, is the best for thick walls within contouring.

4.2.2.4 Strategy E: The best for thick walls-without contouring.

In figure 4.6 it is observed that strategy E has the lowest deviation in all direction that is X,Y and Z. Therefore, it can be concluded that Strategy E which has a 67 degree incremental rotation angle, is the best for thin walls within contouring.

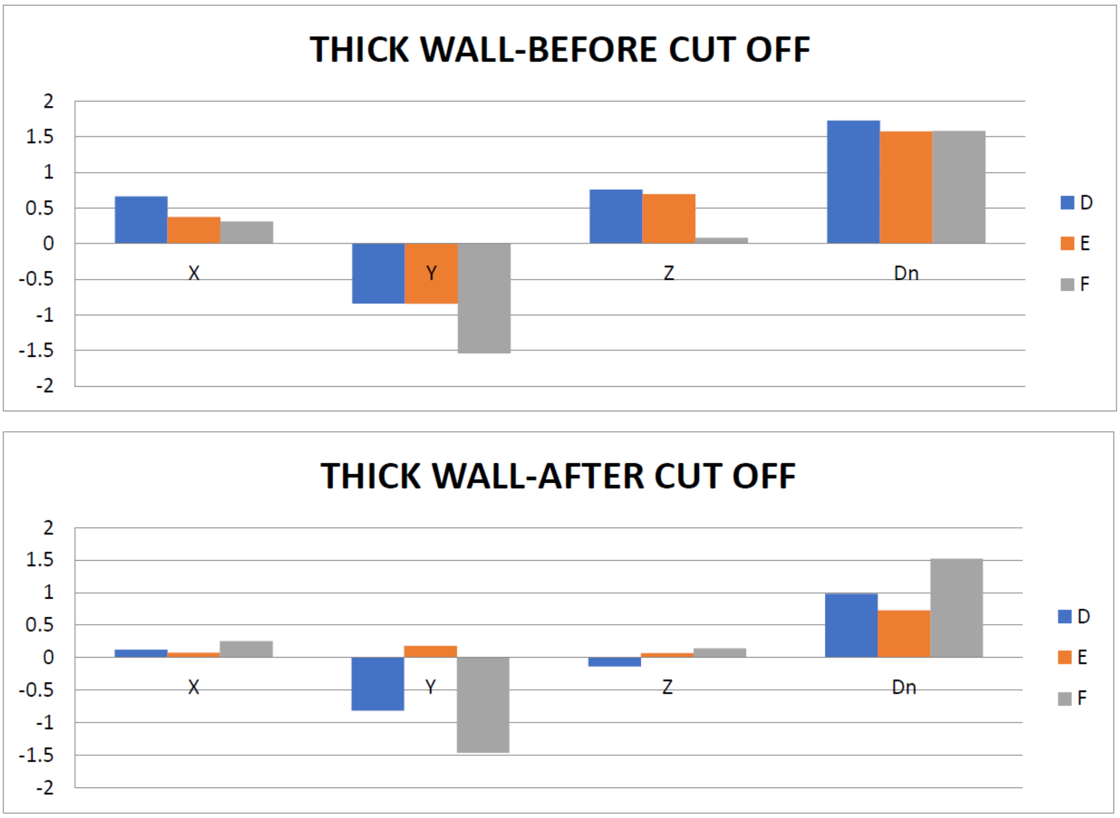

Figure 4.6: Comparison of strategies in without contouring thick wall, before & after cut off.

4.2.3 Summary of the Observations

The below table represents a brief summary of the result:

Table 4.6: Recommended scanning strategy to get the least deviation after cut-off from the build plate.

FEATURE	CONTOURING	NON-CONTOURING
THICK WALL	C(0-10)	E(57-67)
THIN WALL	C(0-10)	NOT RECOMMENDED

4.3 Surface Roughness Analysis

The result from the surface area roughness analysis is presented in this section. It includes surface area parameters, tolerance limits and anomalies.

4.3.1 Acquisition of Surface Area Roughness

The average non-measured points (NMP) ratio for each set of surface roughness acquisition is shown in table 4.7. The values are calculated using 12 measurements which have been done on inclined bars. Except the samples with contouring step included in scanning strategy (samples labeled A, B and C), the measurements needed to be iterated few times to get the best possible results due to the non-similarity of topographies. As it can be seen in this table, the surfaces of contoured parts are much easier to be measured; especially by taking into consideration the fact that the results for non-contoured samples are achieved by several iterations. The specific topography of surfaces in non-contoured parts with very steep valleys and very dark and non-reflective surface, due to severe rusting, causes these measurements a tedious task.

Table 4.7: Non measured points percentage according to the scanning strategies.

	Contouring		**Without Contouring**	
NMP%	4.89		13.10	
	Upside	**Downside**	**Upside**	**Downside**
NMP%	2.88	6.89	10.90	13.11

The missing points are mostly located at steep angles on the surface which cannot be detected by the optical microscope.
In figures 4.7 and 4.8 The smoothest and roughest surfaces among 48 measurements are shown respectively. The difference of topography is crystal clear between these surfaces.

4.3.2 Surface Roughness Parameters Values

In this section the values of surface roughness parameters are listed completely. The parameters of interest are arithmetic mean height(Sa), root square mean height(Sq), kurtosis(Sku) and skewness(Ssk).

4.3.2.1 Consistency of Surface Roughness Values

We have printed two parts for each strategy; so if the results from the same strategy show good consistency, they are more reliable. As it can be seen in figure 4.9, the consistency among the arithmetic mean height values are very good. There is just notable difference on the upside of 45 degree inclined bar in "B" sample which can be ignored. Despite the consistent results of Sa, kurtosis values show more difference. However, regarding the fact that Sku is more sensitive to deep valleys and spikes, we can consider the kurtosis results sufficiently consistent to make an average of them

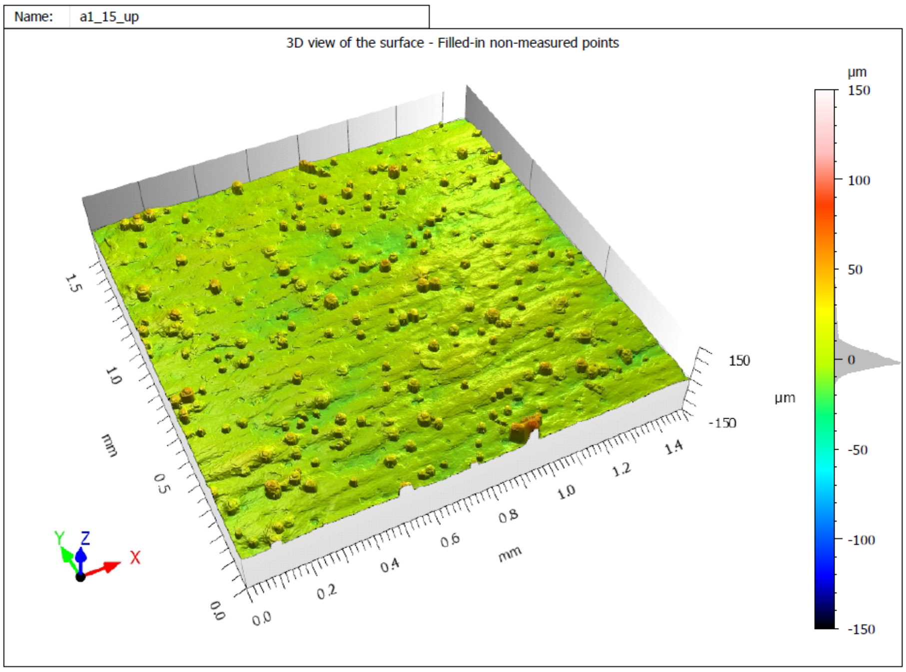

Figure 4.7: 3D map of upside surface of 15 degree slant bar in sample A_1.

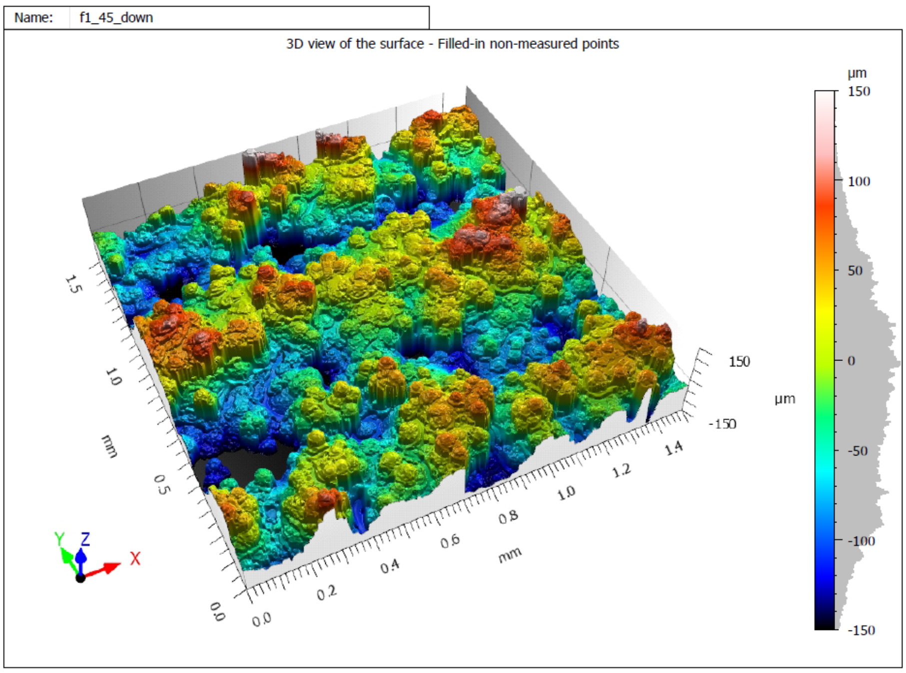

Figure 4.8: 3D map of downside surface of 45 degree slant bar in sample F_1.

(see figure 4.10). In upcoming results, the parameters measured in two samples are averaged and then the averaged amount is used to analyse the surface roughness parameters.In table 4.8 the average results for all samples are listed.

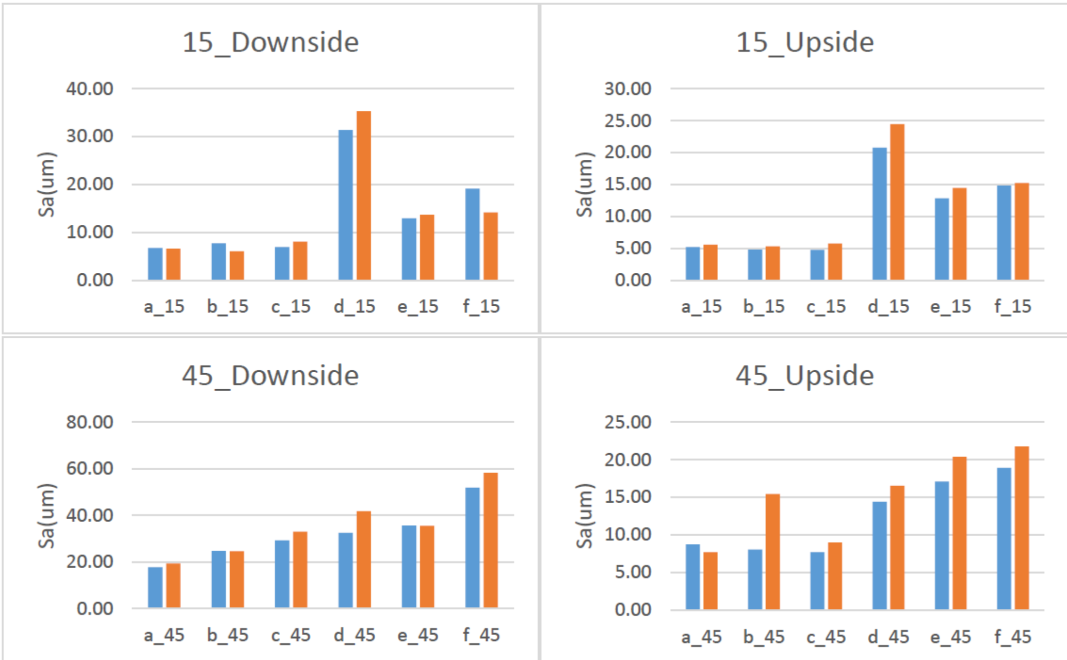

Figure 4.9: Arithmetic mean height of samples.Two parts are printed with each strategy and the Sa values for each strategy are shown next to each other.

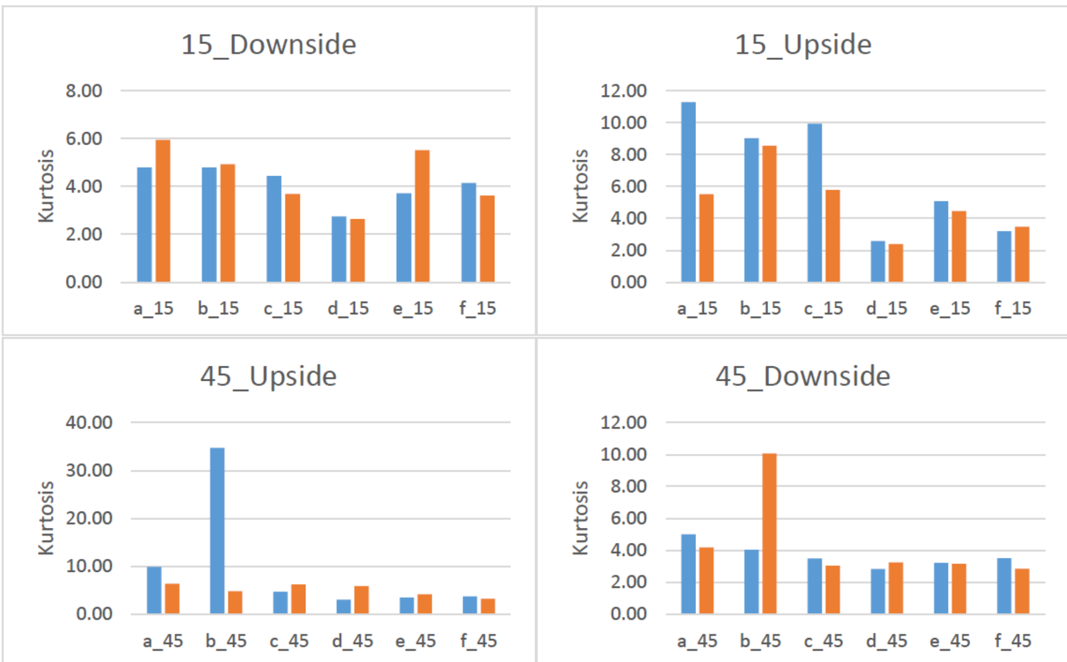

Figure 4.10: Kurtosis values of samples.Two parts are printed with each strategy and the Sa values for each strategy are shown next to each other.

Table 4.8: Average amount of surface roughness parameters for both sides of inclined bars.

	Sa	Sq	Sku			Sa	Sq	Sku
	µm	µm	<no unit>			µm	µm	<no unit>
A-15-D	6.65	9.12	5.37		A-45-D	18.65	24.73	4.59
B-15-D	6.86	9.27	4.86		B-45-D	24.72	33.34	7.05
C-15-D	7.46	9.74	4.06		C-45-D	31.19	39.45	3.25
D-15-D	33.33	40.72	2.70		D-45-D	37.21	46.22	3.02
E-15-D	13.26	17.01	4.62		E-45-D	35.66	45.39	3.18
F-15-D	16.63	21.51	3.88		F-45-D	55.12	69.07	3.17
A-15-U	5.36	7.65	8.40		A-45-U	8.20	11.56	8.08
B-15-U	5.02	7.39	8.79		B-45-U	11.73	16.94	19.74
C-15-U	5.23	7.45	7.87		C-45-U	8.31	11.18	5.44
D-15-U	22.60	27.41	2.48		D-45-U	15.48	20.35	4.42
E-15-U	13.63	17.50	4.77		E-45-U	18.75	24.05	3.79
F-15-U	15.02	19.20	3.33		F-45-U	20.35	25.79	3.45

4.3.2.2 With Contouring Vs. Without Contouring

The surface roughness of contoured parts are explicitly lower than corresponding ones without contouring (see figure 4.11). On the other hand, while the Sa values show an obvious distinction; the kurtosis values of upsides are a bit higher in contoured parts. This difference is more evident over the upsides of the inclined bars.In other words, upsides of samples with contouring are more spiky than ones without contouring (see figure 4.12).

4.3.2.3 Upside Vs. Downside

As it can be seen in figure 4.11, the surface roughness on downside of both 15 degree and 45 degree inclined bars are higher than roughness on upsides. This difference is much more obvious on 45 degree inclined bars. It is worth mentioning the Sa value on the upside of "E" samples which is a bit higher than their downside; because regarding the high level of consistency in Sa values for these samples(see figure 4.9), it is not related to an error in making an average.

In figure 4.10 the kurtosis values are shown. In all samples which contouring step was included in their scanning strategies the Sku is clearly higher on upsides of the bars(Samples "A","B" and "C"). Even the 45 degree inclined bars on samples which have not contoured, show higher Sku value on upsides but this parameter on 15 degree inclined bars on "D","E" and "F" does not follow this trend.

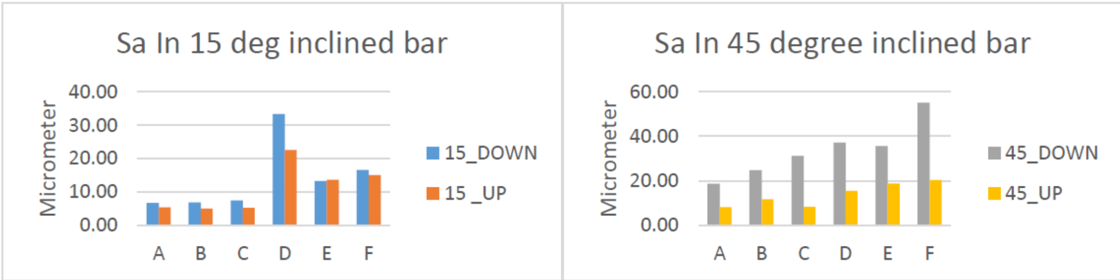

Figure 4.11: Arithmetic mean height on downside Vs. upside of the bars.

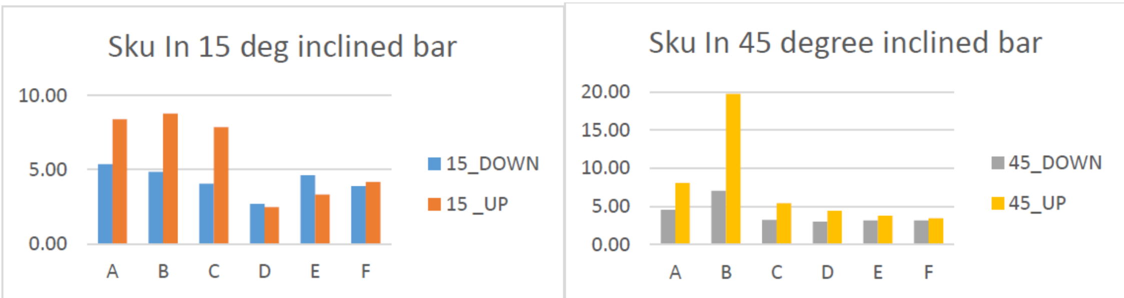

Figure 4.12: Kurtosis values on downside Vs. upside of the bars.

4.3.2.4 Best Scanning Strategy Regarding the Surface Roughness

By considering the arithmetic mean height values on both sides of inclined surfaces, the recommended scanning strategies for 15 degree and 45 degree are listed in table 4.9.

Table 4.9: Recommended scanning strategy to get the least surface roughness.

FEATURE	CONTOURING	NON-CONTOURING
15 degree inclined surfaces	A(0-180)	E(57-67)
45 degree inclined surfaces	A(0-180)	E(57-67)

5

Discussion

In this chapter, the observations and results are analysed. Moreover, the probable basic reasons of those results in connection to former studies are mentioned.

5.1 Geometry Deviations

5.1.1 Simulation Vs. Actual Distortions of Artifacts

Since the strategies with contouring could not be simulated by Ansys-Additive; we only have three simulations that can be compared with printed parts. In figure 5.1 the overall deviation of representative points on thin and thick walls are listed beside the same parameter achieve by simulation(here, the overall deviations have been considered and compared). The more comprehensive data is shown in the annex While the overall deviations of thick walls are comparable to overall deviation of thin walls in all three scanning strategies, the actual values measured on thick wall are much higher than results from simulation in all cases. Even an accordance between the actual and simulation results cannot be found. This inconsistency can be caused for several reasons. For example, we couldn't run the calibration simulations to adjust the proper SSF and anisotropic coefficients. Moreover, the software results should be dependent to the ratio between voxel size and layer thickness in cases we consider the effect of scanning patterns. That is in these simulations a voxel thickness of 0.5 mm (almost 17 times of a layer thickness)has been analysed in each step of simulation; while the scanning pattern of each layer differs to the consecutive one.

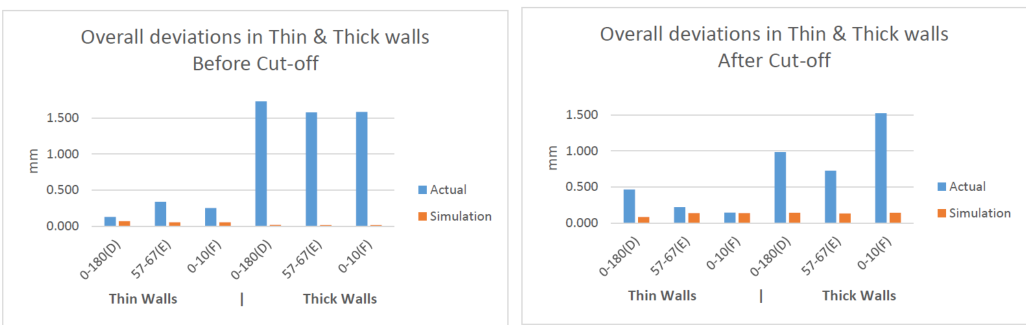

Figure 5.1: Comparison of actual and simulated overall distortions of representative points on thin and thick walls. Left: The values before cut-off from build plate. Right: The values after cut-off from build plate.

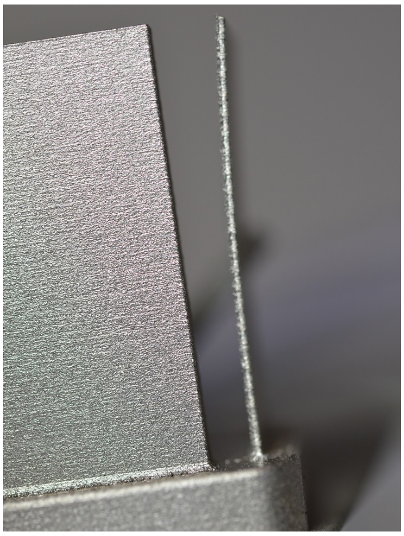

Figure 5.2: Severe distortion of thin wall printed by strategy "C"(10 degree rotation with contouring).

5.1.2 Thickness Limit to Print H13 Tool Steel

Although C strategy(the one with 10 degree hatch rotation angle) gave us the least amount of deviation for thin walls; this statement is limited to the features with the thickness of at least 0.5 mm and the maximum height of 20 mm(the Z coordination of measured points on thin walls). As it can be seen in figure 4.3, although with "C" strategy the thin wall has been printed to the full desired height; it has distorted clearly. As a conclusion, printing thin features with a thickness of 0.5mm and a height of taller than 20 mm definitely will fail; whether with contouring or without contouring as a part of scanning strategy.

5.1.3 Best Hatch Rotation Angle

As mentioned earlier, several researchers has studied different hatch rotations angles in both raster and island scanning patterns to find the optimum rotation angle which yields the lowest residual stresses. 67° has been mentioned as the optimum hatch rotation angle in many papers as by this value the number of layers until the vector direction repeats is the highest value. However, J.H.Robinson et. al.[75] concluded that 10° is a better choice as hatch rotation angle since the number of layers until the vector direction repeats within 10° of the initial vector direction is much higher than 67 degree (see figure 5.3, this value is 16 layers while it is just 8 layers for 67° hatch rotation angle). This calculation was based on the following assumptions:

- Only integer values are considered.
- Hatch vectors will follow a raster pattern, i.e. subsequent vectors will have a rotation of 180° resulting in a direction change.
- The maximum hatch angle rotation is 90°. Any rotation angle above this can be considered to be equal to 180°-t; and therefore an acute angle, rotating in the opposite direction.
- Because of the above assumption, any angles to 180° will be converted to their

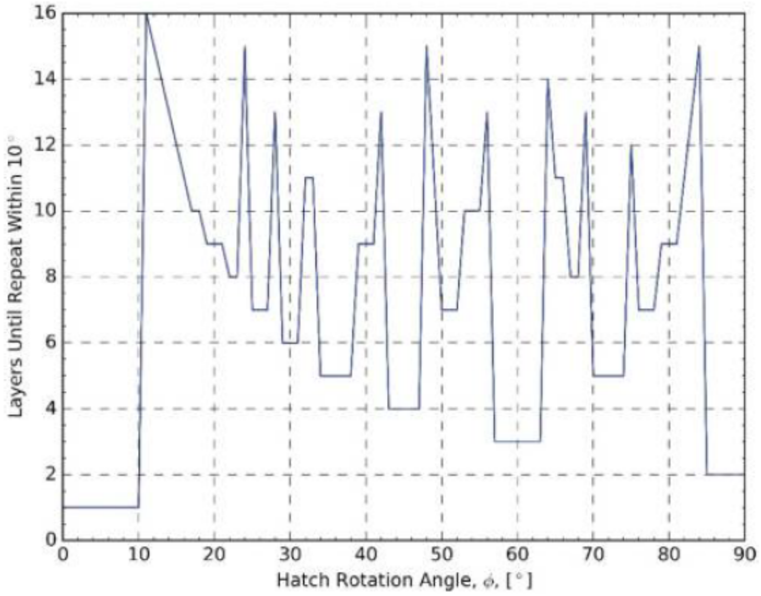

Figure 5.3: Number of layers until the scanning vector direction repeats within 10° according to various hatch rotation angles[75].

obtuse or acute equivalent.

- When calculating the angle between scan vectors the smallest angle will be chosen, i.e. acute angles are forced.

So with 10° rotation in consecutive layers we impose less scanning vectors in the same direction than using 67° for a certain height of build; that is, it distributes the heat source and residual stresses more evenly in the part. This might be the main reason that "C" gives us the least distortions among strategies that includes the contouring step. Among strategies without contouring step, strategy "E" with 67° hatch rotation angle gives better results than strategy "F" which has 10° rotation in each layer. However the difference between E and F is not as huge as different deviations that we got by A,B and C strategies(see figure 4.6).

5.2 Surface Roughness

5.2.1 Different Topography of Upside and Downside Surfaces

The kurtosis parameter on upside surfaces of slants bars are higher than downside ones. This difference is much evident among strategies with contouring step. This seems more meaningful when we consider the fact that higher kortosis represents a more spiky surface. In other words, downside surfaces are more bumpy than upside surfaces due to semi-melted powder particles stuck to the surface. The phenomenon happens because of built-up heat in the part that affect the surrounding particles and partially melt them. As the inclination angle decreases, the heat conduction to the build plate becomes more difficult and hence more partially melted particles stick to the surfaces, mainly to the downside surface, because of the heat conduction

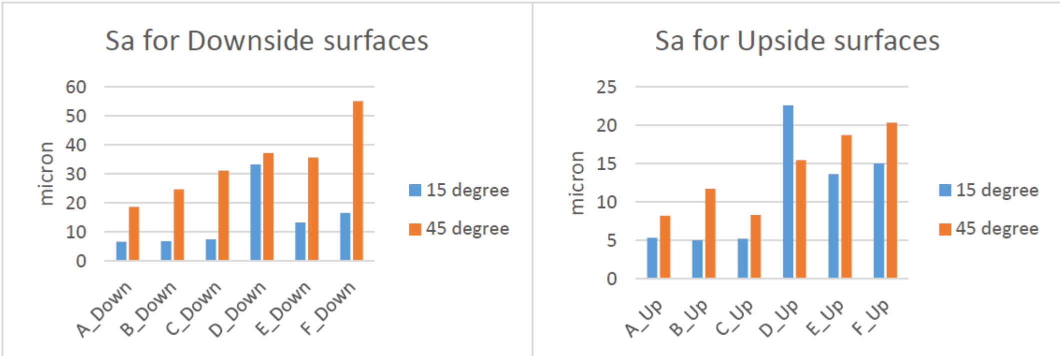

Figure 5.4: Arithmetic mean height on downside and upside surfaces.

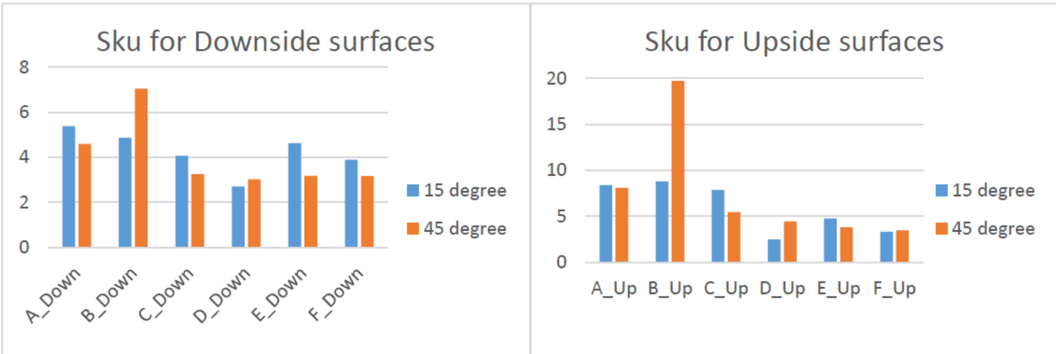

Figure 5.5: Kurtosis of downside and upside surfaces.

direction. This phenomenon is the main reason that makes the downside surfaces rougher than upside ones. These findings are in good accordance with former studies.

5.2.2 Effect of Inclination Angle on Surface Roughness

- Arithmetic mean height as one of the most important parameters which describes the surface roughness is higher on surfaces with 45 degree inclination than 15 degree slant surfaces. The only exception for this observation is higher Sa on the upside surface of samples printed by "D" strategy(see figure 5.4). The main reason to have a rougher surface on down-skins should be because of partially melted powder particles which sticks to the surface.
- By comparing the kurtosis parameters on surfaces with 15 and 45 degree inclination, no obvious trend, like we saw about Sa, is observed. In overall, we could roughly consider 15 degree slant surfaces more spiky than 45 degree ones; however this judgement is not completely accurate and needs more data to elaborate(see figure 5.5).

5.3 Contouring or No-Contouring?

To recapture the scientific questions stated in Section 1.4, these are recited in this section along with comments.

- **How much surface roughness is affected in the case of omitting the contouring step?**

Considering the Sa parameter as the surface roughness parameters(see figure 4.11) reveals that without contouring we get rougher surfaces on all slant surfaces. While the range of Sa for 15 degree inclined surfaces is roughly between 5-10 micrometer for A,B and C strategies; this value fits in a range of 15-30 micron for non-contoured parts(D,E,F). Although the Sa values ratio of non-contoured parts are 2-5 times of Sa in contoured parts, we should remember that components produced by SLM process are not used as the end-use product. Moreover, the lowest Sa value achieved in these samples is around 5 micrometer which is much higher than a machined surface. In 45 degree slant bars, the Sa values of non-contoured samples are more or less 2 times of Sa values on corresponding contoured parts. These level of surface roughness are not acceptable in industry.

- **How much geometrical variation is noticed from the planned scanning strategies?**

By comparing the figures 4.5 and 4.6 we cannot get a clear trend about the effect of contouring on the deviation of thick wall point. In 180 degree and 67 degree hatch rotation angle strategy, we get higher overall distortion by contouring while in 10 degree hatch rotation angle the contouring step gives the least amount of distortion. It might be due to the complexity of residual stress state in the part. The only obvious conclusion about these strategies is that strategy "C" gives the best results in term of achieving the least amount of distortion after cutting the parts from the build plate.

6
Conclusion

In this project the effect of three different hatch rotation angles in raster scanning pattern on surface roughness and geometrical deviations in artifacts made of H13 tool steel was experimentally investigated. The results from printed parts were compared to the simulation results achieved by Ansys- Additive software version 2019R1. No consistency was observed among the experimental and simulation results which might be due to un-calibrated simulations and the hardware limitations which enforced us to consider the voxel thickness a multiple times larger than layer thickness.

The parameters related to the scanning strategies play an important role which helps to achieve the best possible geometry and surface roughness. Despite other papers which have considered 67 degree hatch rotation angle as one of the most optimum ones; in this project, from the results that are obtained, it can be best concluded that hatch rotation angle of 10 degree (strategy C) is the best in terms of achieving geometrical accuracy. The main reason of this finding might be related to the fact that with 10 degree rotation more layers should be printed until the scan direction falls in vicinity of the first layer scanning direction(with a range of 10 degree).

In terms of lower surface roughness, it can be concluded that hatch angle rotation of 180 degrees (strategy A) proved to the best. However, it is important to note that these results are with respect to H13 Tool Steel material printed in SLM125 machine in RISE IVF.

Bibliography

[1] I. Gibson, D. W. Rosen, B. Stucker, Additive Manufacturing Technologies-Rapid Prototyping to Digital Manufacturing Methods

[2] A. Bandyopadhyay & S. Bose, Additive manufacturing, CRC Press, Taylor & Francis Group, 2016.

[3] 10.04.http://s550682939.onlinehome.fr/CommissionsThematiques/DocCom Thematiques/ EPMA_Additive_Manufacturing.pdf

[4] H. Ali, H. Ghadbeigi, K. Mumtaz, Effect of scanning strategies on residual stress and mechanical properties of Selective Laser Melted Ti6Al4V, Materials Science and Engineering: A, Volume 712, 2018, Pages 175-187, ISSN 0921-5093, https://doi.org/10.1016/j.msea.2017.11.103.

[5] J. P. Kruth, J. Deckers, E. Yasa, R. Wauthle, Assessing and comparing influencing factors of residual stresses in selective laser melting using a novel analysis method, Proc. Inst. Mech. Eng. Part B J. Eng. Manuf. 226 (2012) 980-991.

[6] P. Mercelis, J. P. Kruth, Residual stresses in selective laser sintering and selectivelaser melting, Rapid Prototyp. J. 12 (2006) 254-265.

[7] ASTM Standard. Standard terminology for additive manufacturing technology,Vol. 10.04.

[8] Gartner AM report. Information on http://www.gartner.com/document/2598 122, Accessed 16 June 2014.

[9] AM Platform: Additive Manufacturing Strategic Research Agenda: Release 2014.Available online: http://www.rm-platform.com/linkdoc/AM20SRA20-20February202014.pdf Access 5 Mar 2015.

[10] Wohlers TT (2014) Wohlers report 2014: additive manufacturing and 3D print-ing state of the industry: annual wordwide progress report. Fort Collins, WohlersAssociates.

[11] H.K. Rafi, T.L. Starr, B.E. Stucker, A comparison of the tensile, fatigue andfracture behavior of Ti-6Al-4V an 15-5 PH stainless steel parts made by selectivelaser melting, Int. J. Adv. Manuf. Technol. 69 (2013) 1299-1309.

[12] A. Yadollahi, N. Shamsaei, S.M. Thompson, A. Elwany, L. Bian, Mechanical andmicrostructural properties of selective laser melted 17-4 PH stainless steel, in: ASMEInternational Mechanical Engineering Conference and Exposition, 2015.

[13] Y. Ning, Y. S. Wong, J. Y. H. Fuh, and H. T. Loh, An approach to minimizebuild errors in Direct Metal Laser Sintering, IEEE Trans, Autom. Sci. Eng., 3(1)(2006) 73-80.

[14] Y. Ning, Y. S. Wong, J. Y. H. Fuh, Effect and control of hatch length on materialproperties in Direct Metal Laser Sintering process, Proc. Inst. Mech. Eng., Part B,219(1) (2005) 15-25.

[15] R. Paul and S. Anand, Material shrinkage modeling and form error prediction inadditive manufacturing processes, Proceedings of the 41st NAMRC 2013, Madison,WI.

[16] R. Wang, L. Wang, L. Zhao and Z. Liu, Influence of process parameters on partshrinkage in SLS, Int. J. Adv. Manuf. Technol. 33(5-6) (2007) 498-504.

[17] X. C. Wang, T. Laoui, J. Bonse, J.P. Kruth, B. Lauwers and L. Froyen, Direct Selective Laser Sintering of Hard Metal Powders: Experimental Study and Simula-tion, Int. J. Adv. Manuf. Technol., 19(5) (2002) 351-357.

[18] X. Wang, Calibration of Shrinkage and Beam Offset in SLS Process, Rapid Prototyping J., 5(3) (1999) 129-133.

[19] K. Senthilkumaran, P.M. Pandey and P.V.M. Rao, New Model for Shrinkage Compensation in Selective Laser Sintering, Virtual Phys. Prototyping, 4(2) (2009)49-62.

[20] P. Jacobs, The Effects of Random Noise Shrinkage on Rapid Tooling Accuracy,Mater. Des., 21(2) (2000) 127-136.

[21] H. Bikas, P. Stavropoulos, G. Chryssolouris, Additive manufacturing methods and modelling approaches: a critical review, Int. J. Adv. Manuf. Technol. 83(2016) 389-405.

[22] H. Pohl, A. Simchi, M. Issa, H. Dias, Thermal stresses in direct metal laser sintering, Proc. SFF Symp. (2001), pp. 366-372.

[23] J. P. Kruth, L. Froyen, J. Van Vaerenbergh, P. Mercelis, M. Rombouts, B.Lauwers, Selective laser melting of iron-based powder, J. Mater. Process. Technol.149 (2004) 616-622.

[24] J. Robinson, I. Ashton, E. Jones, P. Fox, C. Sutcliffe, The effect of hatch angle rotation on parts manufactured using selective laser melting, Rapid Prototyp. J.,25(2) (2019) 289-298.

[25] S.A. Sillars, C.J. Sutcliffe, A.M. Philo, S.G.R. Brown, J. Sienz, N.P. Lavery,The threeprong method: a novel assessment of residual stress in laser powder bed-fusion, Virtual Phys. Prototyp. 13 (2018) 20-25.

[26] M. F. Zaeh, G. Branner, Investigation on residual stresses and deformations in selective laser melting, Prod. Eng. 4(2009) 35-45.

[27] D. Buchbinder, W. Meiners, N. Pirch, K. Wissenbach, J. Schrage, Investigation on reducing distortion by preheating during manufacture of aluminum componets using selective laser melting, J. Laser Appl. 26 (2014) 012004.

[28] I. Yadroitsava, S. Grewar, D. Hattingh, I. Yadroitsev, Residual stress in SLM Ti6Al4V alloy specimens, Mater. Sci. Forum 828-829 (2015) 305-310.

[29] M. Shiomi, K. Osakada, K. Nakamura, T. Yamashita, F. Abe, Residual stress within metallic model made by selective laser melting process, CIRP Ann.-Manuf.Technol. 53 (2004) 195-198.

[30] J.P. Kruth, M. Badrossamay, E. Yasa, J. Deckers, L. Thijs, J. Van Humbeeck,Part and material properties in selective laser melting of metals, in: Proceedings of the 16th International Symposium on Electromachining (ISEM XVI). Shanghai,China, 2010.

[31] M.F. Zaeh, G. Branner, Investigations on residual stresses and deformations in selective laser melting, Prod. Eng.: Res. Dev. Ger. 4 (2010) 1.

[32] A.H. Nickel, D.M. Barnett, F.B. Prinz, Thermal stresses and deposition patterns in layered manufacturing, Mater. Sci. Eng.: A 317 (1-2) (2001) 59-64.

[33] A.V. Gusarov, M. Pavlov, I. Smurov, Residual stresses at laser surface remelting and additive manufacturing, Phys. Procedia 12 (2011) 248-254.

[34] B. Cheng, S. Shrestha, K. Chou, Stress and deformation evaluations of scanning strategy effect in selective laser melting, Addit. Manuf. (12, Part B) (2016) 240-251.

[35] I.A. Robers, Investigation of residual stresses in the laser melting of metal powder in Additive Layer Manufacturing, University of Wolverhampton, 2012, p.246.

[36] L. Parry, I.A. Ashcroft, R.D. Wildman, Understanding the effect of laser scan strategy on residual stress in selective laser melting through thermos-mechanical simulation, Addit. Manuf. (12, Part A) (2016) 1-15.

[37] M. F. Zaeh and G. Branner: Prod. Eng. Res. Devel., 2010, vol. 4, pp. 35-45.

[38] J. P. Kruth, J. Deckers, E. Yasa, and R. Wauthle: Proc. Inst. Mech. Eng. B,2012, vol. 226, pp. 980-991.

[39] A.J. Dunbar, et al., Development of experimental method for in situ distortion and temperature measurements during the laser powder bed fusion additive manufacturing process, Addit. Manuf. (12, Part A) (2016) 25-30.

[40] K. Guan, Z. Wang, M. Gao, X. Zeng, Effect of processing parameters on tensile properties of selective laser melted 304 stainless steel, Mat. And Des. 50 (2013)581-586.

[41] M.F. Zaeh, G. Branner, Investigations on residual stresses and deformations in selective laser melting, Prod. Eng. 4 (2009) 35-45.

[42] J. Robinson, I. Ashton, P. Fox, E. Jones, C. Sutcliffe, Determination of the effect of scan strategy on residual stress in laser powder bed fusion additive manufacturing,Additive Manuf. 23 (2018) 13-24.

[43] E. Yasa: Dissertation, Katholieke Universiteit Leuven, Belgium, 2011.

[44] Y. Lu, S. Wu, Y. Gan, T. Huang, C. Yang, L. Junjie and J. Lin, Study on the microstructure, mechanical property and residual stress of SLM Inconel-718 alloy manufactured by differing island scanning strategy, Optics & Laser Technology 75(2015) 197-206.

[45] Amanda S. Wu, Donald W. Brown, Mukul Kumar, Gilbert F. Gallegos and-Wayne E. King, An experimental investigation into additive manufacturing induced residual stresses in 316L stainless steel, Metallurgical and Materials Transactions A,45A (2014) 6260-6270.

[46] S. Mohanty, J. H. Hattel, reducing residual stresses and deformations in selective laser melting through multilevel multi scale optimization of cellular scanning strategy, Proc. of SPIE, Vol.9738 (2016) 97380Z-1-97380Z-12.

[47] D. Hagedorn-Hansen, M.B. Bezuidenhout, D.M. Dimitrov and G.A. Oosthuizen,The effect of selective laser melting scan strategies on deviation of hybrid parts,South African J. of Industrial Engineering 28(3) (2017) 200-212.

[48] B. Qian, Y.-s. Shi, Q.-s. Wei, H.-b. Wang, The helix scan strategy applied tothe selective laser melting, Int. J. Adv. Manuf. Technol. 63 (5-8) (2012) 631-640.

[49] ASME Y14.5-2009 Dimensioning and Tolerancing. ASME, 2009.

[50] K. Dalgarno, Materials research to support high performance RM parts. Rapid Manuf. 2nd International conference, Loughborough Univ., 9-12 July, 2007, pp.147-156.

[51] Strano G., Hao L., Everson R.M., Evans K.E., Surface roughness analysis,modeling and prediction in selective laser melting, J. Mater. Process Technol. 213(4)(2013) 589-597.

[52] F. Kaji, A. Barari, Evaluation of the surface roughness of additive manufacturing parts based on the modelling of cusp geometry, IFAC-Papers OnLine 58-3 (2015)658-663.

[53] S. Sikder, A. Barari, H. Kishawy, Global adaptive slicing of NURBS based sculp-tured surface for minimum texture error in rapid prototyping, Rapid Prototyping journal, 21(6) (2014).

[54] S. Sikder, A. Barari, H. Kishawy, Effect of adaptive slicing on surface integrity in additive manufacturing, ASME International Design Engineering Technical Confer-ences & Computers and Information in Engineering Conference, DETC/CIE 2014,Aug 19-22, 2014, Buffalo, NY, US.

[55] S. Jamiolahmadi, A. Barari, Surface topography of AM parts using a finite difference approach, ASME Transactions- J. Manuf. Sci. and Eng., Vol.136(6)(2014) 061009-18.

[56] S. Jamiolahmadi, A. Barari, Surface roughness model for AM parts using a finite difference method, ASME Int. Mechanical Engineering Congress & Exposition,IMECE 2014, Montreal, Canada.

[57] I. Koutiri, E. Pessard, P. Peyre, O. Amlou, T. De Terris, Influence of SLM-process parameters on the surface finish, porosity rate and fatigue behavior of as-built Inconel 625 parts, J. Mat. Proc. Technol. 255 (2018) 536-546.

[58] M. Mohammadi, H. Asgari, Achieving low surface roughness ALSi10Mg-200Cparts using direct metal laser sintering, Additive Manufacturing 20 (2018) 23-32.

[59] P.B. Bacchewar, S.K. Singhal, P.M. Pandey, Statistical modeling and optimization of surface roughness in the selective laser sintering process, Proc. Inst. Mech.Eng. Part B: J. Eng. Manuf. 221 (2007) 35-52.

[60] Y. tian, D. Tomus, P. Rometsch, X. Wu, Influence of processing parameterson surface roughness of Hastelloy X produced by selective laser melting, Additive Manufacturing 13 (2017) 103-112.

[61] F. Wang, X.H. Wu, D. Clark, On direct laser deposited hastelloy X: dimension,surface finish, microstructure and mechanical properties, Mater. Sci. Technol. 27(1)(2011) 344-356.

[62] F. Cabanettesa, A. Jouberta, G. Chardona, V. Dumasa, J. Recha, C. Grosjeanb, Z. Dimkovskic, Topography of as built surfaces generated in metal additive manufacturing: A multi scale analysis from form to roughness, Precision Engineering 52 (2018) 249–265.

[63] A. Thompson, N. Senin, C. Giusca, R.K. Leach, Topography of selectively laser melted surfaces: a comparison of different measurement methods. CIRP Ann-Manuf Technol; 2017.

[64] N. Senin, A. Thompson, R.K. Leach, Characterisation of the topography of metal additive surface features with different measurement technologies. Precis Eng 2016.

[65] R. K. Leach, Optical measurement of surface topography, Springer, Berlin,2011.

[66] T. Dam, N. Ravirujiphant, Defining Machine Capability for Metals Additive Manufacturing Machines, Master's thesis, Chalmers University of Technology, 2018.

[67] L. Newton, N. Senina, C. Gomeza, R. Danzld, F. Helmlid, L. Blunt, R. Leach, Areal topography measurement of metal additive surfaces using focus variation microscopy, Additive Manufacturing 25 (2019) 365–389.

[68] R. K. Leach, Characterization of areal surface texture, Springer, Berlin,2013.

[69] S. Kolossov, E. Boillat, R. Glardon, P. Fischer, and M. Locher. 3D FE simulation for temperature evolution in the selective laser sintering process. International Journal of Machine Tools and Manufacture, 44(2- 3):117–123, February 2004.

[70] L. Dong, a. Makradi, S. Ahzi, and Y. Remond. Three-dimensional transient finite element analysis of the selective laser sintering process. Journal of Materials Processing Technology, 209(2):700–706, January 2009.

[71] M. Matsumoto, M. Shiomi, K. Osakada, and F. Abe. Finite element analysis of single layer forming on metallic powder bed in rapid prototyping by selective laser processing. International Journal of Machine Tools and Manufacture, 42(1):61–67, January 2002.

[72] Ansys 2019 R1, Ansys Inc, January 2019.

[73] Materials data sheet, Tool Steel 1.2344 / A681 H13 / H13, SLM Solutions, Lubeck, Deutchalnd.

[74] ATOS user manual hardware, ATOS III triple scan, Rev.02, GOM GmbH, Braunschweig, 2013.

[75] J. H. Robinson, I. R. T. Ashton, E. Jones, P. Fox and C. Sutcliffe, The effect of hatch angle rotation on parts manufactured using selective laser melting, Rapid Prototyping Journal, Vol. 25 Issue: 2, 289-298, 2019.

A

Appendix

A.1 Slant Cube Geometries and Simulation Results

In this section the geometries of slant cube and the results of preliminary simulations are included.

A.1.1 Geometries of Slant Cube

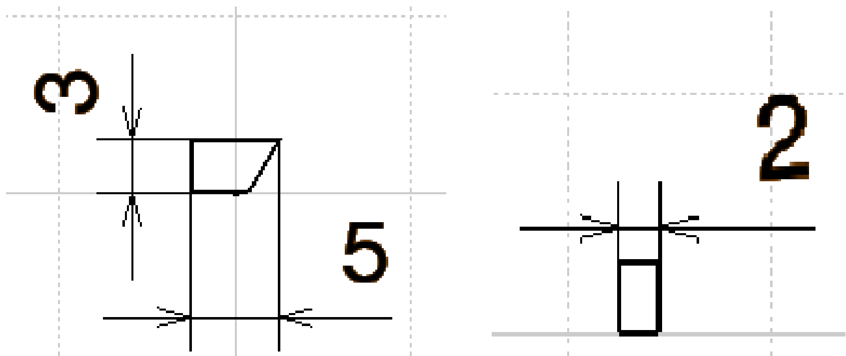

Figure A.1: Left:Front view and Right: Top view of slant cube(dimensions in mm).

A.1.2 Preliminary simulations and results

To figure out the sensitivity of simulations to voxel size, the slant cube was simulated with 4 different voxel sizes but with the same scanning pattern which is chess pattern with default setting identified in Magicmaterials software.

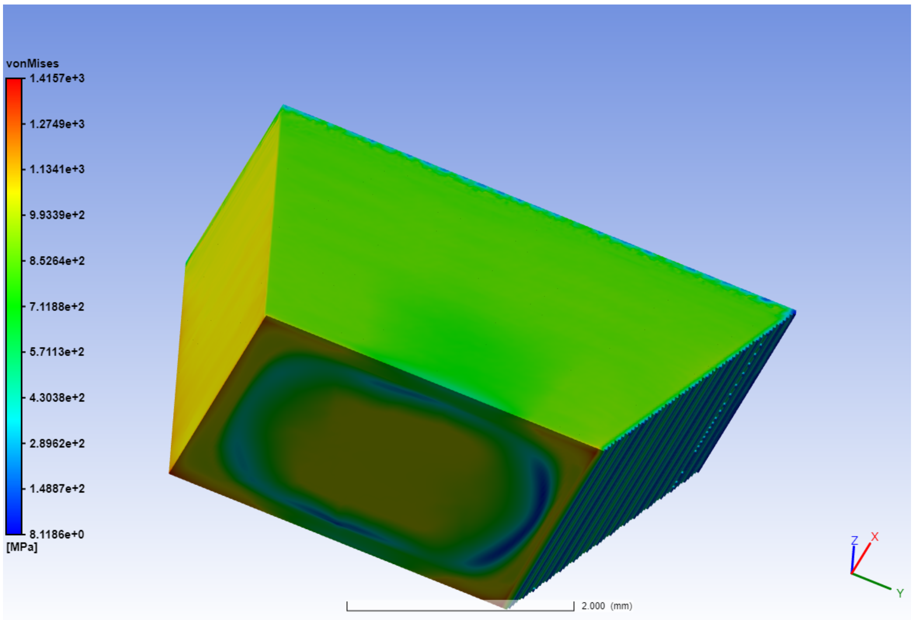

Figure A.2: Von-Mises stress in slant cube with deffault chess pattern as scanning strategy(voxel size of 30 micrometer).

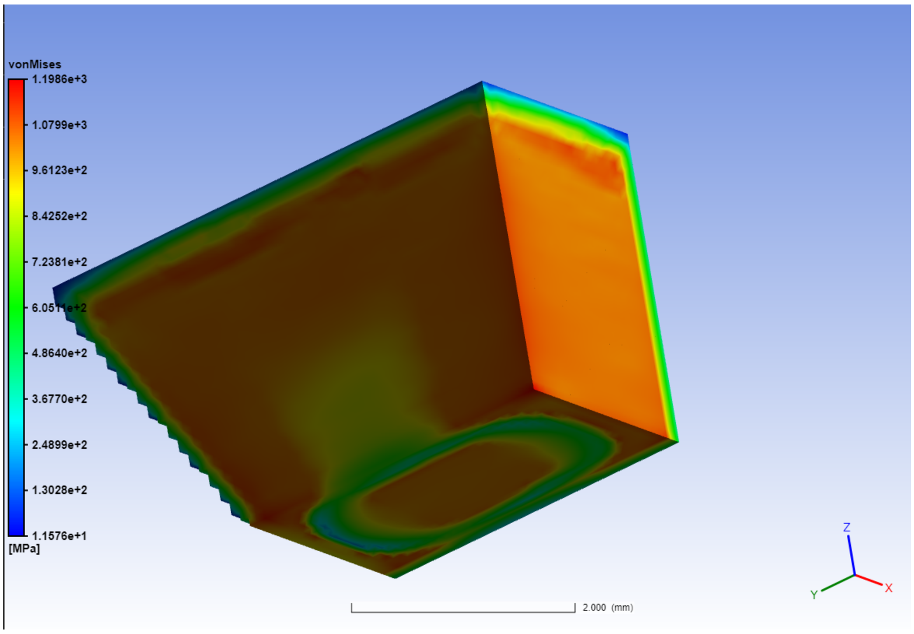

Figure A.3: Von-Mises stress in slant cube with deffault chess pattern as scanning strategy(voxel size of 90 micrometer).

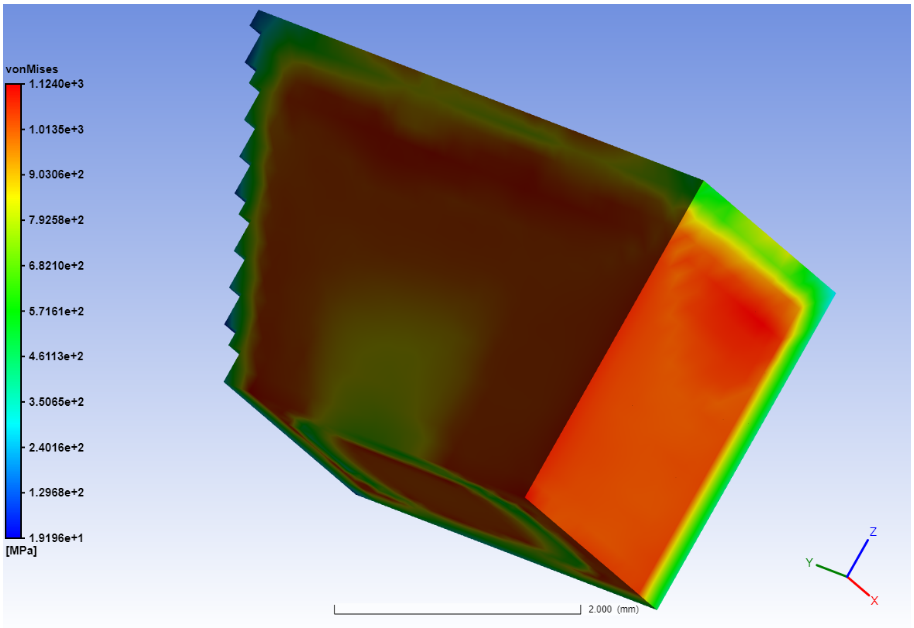

Figure A.4: Von-Mises stress in slant cube with deffault chess pattern as scanning strategy(voxel size of 150 micrometer).

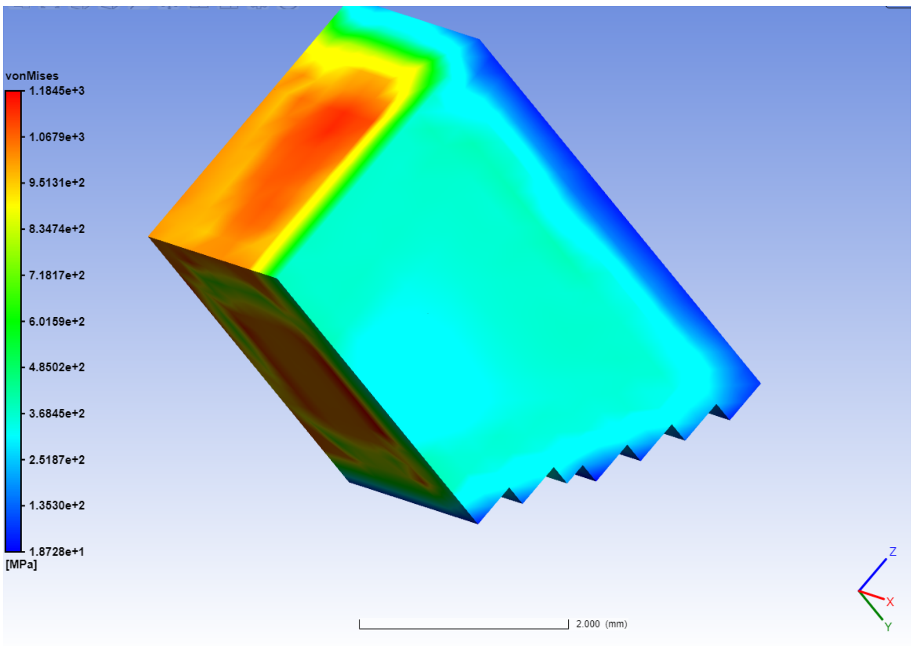

Figure A.5: Von-Mises stress in slant cube with deffault chess pattern as scanning strategy(voxel size of 240 micrometer).

A.2 Statistical Overview of Printed Artifacts

The coordinates of three reference points on thick walls and three reference points on thin walls of artifacts has been recorded before and after cut-off. In this section the results for other 11 samples are reported(Sample A_1 was reported in results section).

Table A.1: Typical statistical overview for A2-before cut off.

Feature	Element	Nominal			Actual			Deviation			
		X	Y	Z	X	Y	Z	dX	dY	dZ	dN
Thick wall	Point 6	-12	-7.5	32.5	-11.804	-9.011	32.531	0.196	-1.511	0.031	1.524
	Point 5	-12	-7	33	-11.683	-9.018	33.011	0.317	-2.018	0.011	2.043
	Point 4	-12	-8	33	-11.683	-9.018	33.011	0.317	-1.018	0.011	1.066
Average								**0.277**	**-1.516**	**0.018**	**1.544**
Thin wall	Point 3	-8	-12.5	25	-8.016	-12.552	25.039	-0.016	-0.052	0.039	0.067
	Point 2	-9	-12.5	25	-9	-12.543	25	0.000	-0.043	0.000	0.043
	Point 1	-8.5	-12.5	24.5	-8.498	-12.559	24.501	0.002	-0.059	0.001	0.059
Average								**-0.005**	**-0.051**	**0.013**	**0.056**

Table A.2: Typical statistical overview for A2-after cut off.

Feature	Element	Nominal			Actual			Deviation			
		X	Y	Z	X	Y	Z	dX	dY	dZ	dN
Thick wall	Point 6	-12	-7.5	32.5	-11.879	-9.008	32.353	0.121	-1.508	-0.147	1.520
	Point 5	-12	-7	33	-11.71	-8.894	33.392	0.290	-1.894	0.392	1.956
	Point 4	-12	-8	33	-11.71	-8.894	33.392	0.290	-0.894	0.392	1.018
Average								**0.234**	**-1.432**	**0.212**	**1.498**
Thin wall	Point 3	-8	-12.5	25	-7.997	-11.922	25.009	0.003	0.578	0.009	0.578
	Point 2	-9	-12.5	25	-8.975	-11.925	25.001	0.025	0.575	0.001	0.576
	Point 1	-8.5	-12.5	24.5	-8.475	-11.923	24.497	0.025	0.577	-0.003	0.578
Average								**0.018**	**0.577**	**0.002**	**0.577**

Table A.3: Typical statistical overview for B1-before cut off.

Feature	Element	Nominal			Actual			Deviation			
		X	Y	Z	X	Y	Z	dX	dY	dZ	dN
Thick wall	Point 6	-12.0	-7.5	32.5	-11.669	-9.004	32.617	0.331	-1.504	0.117	1.544
	Point 5	-12.0	-7.0	33.0	-11.709	-9.016	33.071	0.291	-2.016	0.071	2.038
	Point 4	-12.0	-8.0	33.0	-11.709	-9.016	33.089	0.291	-1.016	0.089	1.061
Average								**0.304**	**-1.512**	**0.092**	**1.548**
Thin wall	Point 3	-8.0	-12.5	25.0	-8.000	-12.707	24.994	0.000	-0.207	-0.006	0.207
	Point 2	-9.0	-12.5	25.0	-8.999	-12.713	24.990	0.001	-0.213	-0.010	0.213
	Point 1	-8.5	-12.5	24.5	-8.427	-12.699	24.453	0.073	-0.199	-0.047	0.217
Average								**0.025**	**-0.206**	**-0.021**	**0.212**

Table A.4: Typical statistical overview for B1-after cut off.

Feature	Element	Nominal			Actual			Deviation			
		X	Y	Z	X	Y	Z	dX	dY	dZ	dN
Thick wall	Point 6	-12	-7.5	32.5	-11.797	-9.025	32.583	0.203	-1.525	0.083	1.540689
	Point 5	-12	-7	33	-11.82	-9.021	32.764	0.180	-2.021	-0.236	2.042679
	Point 4	-12	-8	33	-11.82	-9.021	32.764	0.180	-1.021	-0.236	1.063267
Average								**0.188**	**-1.522**	**-0.130**	**1.549**
Thin wall	Point 3	-8	-12.5	25	-8.014	-12.095	25.004	-0.014	0.405	0.004	0.405262
	Point 2	-9	-12.5	25	-8.998	-12.103	25.005	0.002	0.397	0.005	0.397037
	Point 1	-8.5	-12.5	24.5	-8.502	-12.087	24.513	-0.002	0.413	0.013	0.413209
Average								**-0.005**	**0.405**	**0.007**	**0.405**

Table A.5: Typical statistical overview for B2-before cut off.

Feature	Element	Nominal			Actual			Deviation			
		X	Y	Z	X	Y	Z	dX	dY	dZ	dN
Thick wall	Point 6	-12	-7.5	32.5	-11.445	-8.996	32.409	0.555	-1.496	-0.091	1.598
	Point 5	-12	-7	33	-11.45	-9	32.873	0.550	-2.000	-0.127	2.078
	Point 4	-12	-8	33	-11.455	-9.003	33.1	0.545	-1.003	0.100	1.146
Average								**0.550**	**-1.500**	**-0.039**	**1.607**
Thin wall	Point 3	-8	-12.5	25	-7.996	-12.696	24.995	0.004	-0.196	-0.005	0.196
	Point 2	-9	-12.5	25	-8.976	-12.229	25.06	0.024	0.271	0.060	0.279
	Point 1	-8.5	-12.5	24.5	-8.505	-12.676	24.491	-0.005	-0.176	-0.009	0.176
Average								**0.008**	**-0.034**	**0.015**	**0.217**

Table A.6: Typical statistical overview for B2-after cut off.

Feature	Element	Nominal			Actual			Deviation			
		X	Y	Z	X	Y	Z	dX	dY	dZ	dN
Thick wall	Point 6	-12	-7.5	32.5	-11.771	-9.027	32.576	0.229	-1.527	0.076	1.546
	Point 5	-12	-7	33	-11.675	-9.021	32.946	0.325	-2.021	-0.054	2.048
	Point 4	-12	-8	33	-11.771	-9.04	32.97	0.229	-1.040	-0.030	1.065
Average								**0.261**	**-1.529**	**-0.003**	**1.553**
Thin wall	Point 3	-8	-12.5	25	-8.014	-12.055	25.005	-0.014	0.445	0.005	0.445
	Point 2	-9	-12.5	25	-8.993	-12.059	24.996	0.007	0.441	-0.004	0.441
	Point 1	-8.5	-12.5	24.5	-8.447	-12.044	24.566	0.053	0.456	0.066	0.464
Average								**0.015**	**0.447**	**0.022**	**0.450**

Table A.7: Typical statistical overview for C1-before cut off.

Feature	Element	Nominal			Actual			Deviation			
		X	**Y**	**Z**	**X**	**Y**	**Z**	**dX**	**dY**	**dZ**	**dN**
Thick wall	Point 6	-12	-7.5	32.5	-11.864	-9.011	32.48	0.136	-1.511	-0.020	1.517
	Point 5	-12	-7	33	-11.867	-9.014	32.869	0.133	-2.014	-0.131	2.023
	Point 4	-12	-8	33	-11.856	-9.014	32.887	0.144	-1.014	-0.113	1.030
Average								**0.138**	**-1.513**	**-0.088**	**1.523**
Thin wall	Point 3	-8	-12.5	25	-7.944	-12.753	25.046	0.056	-0.253	0.046	0.263
	Point 2	-9	-12.5	25	-9.406	-12.821	24.117	-0.406	-0.321	-0.883	1.024
	Point 1	-8.5	-12.5	24.5	-8.464	-12.737	24.468	0.036	-0.237	-0.032	0.242
Average								**-0.105**	**-0.270**	**-0.290**	**0.510**

Table A.8: Typical statistical overview for C1-after cut off.

Feature	Element	Nominal			Actual			Deviation			
		X	**Y**	**Z**	**X**	**Y**	**Z**	**dX**	**dY**	**dZ**	**dN**
Thick wall	Point 6	-12	-7.5	32.5	-11.77	-9.014	32.418	0.230	-1.514	-0.082	1.534
	Point 5	-12	-7	33	-11.791	-9.026	33.076	0.209	-2.026	0.076	2.038
	Point 4	-12	-8	33	-11.804	-9.029	33.018	0.196	-1.029	0.018	1.048
Average								**0.212**	**-1.523**	**0.004**	**1.540**
Thin wall	Point 3	-8	-12.5	25	-7.998	-12.612	24.997	0.002	-0.112	-0.003	0.112
	Point 2	-9	-12.5	25	-9.003	-12.646	24.992	-0.003	-0.146	-0.008	0.146
	Point 1	-8.5	-12.5	24.5	-8.498	-12.574	24.491	0.002	-0.074	-0.009	0.075
Average								**0.000**	**-0.111**	**-0.007**	**0.111**

Table A.9: Typical statistical overview for C2-before cut off.

Feature	Element	Nominal			Actual			Deviation			
		X	**Y**	**Z**	**X**	**Y**	**Z**	**dX**	**dY**	**dZ**	**dN**
Thick wall	Point 6	-12	-7.5	32.5	-11.82	-9.013	32.288	0.180	-1.513	-0.212	1.538
	Point 5	-12	-7	33	-11.673	-9.014	33.037	0.327	-2.014	0.037	2.041
	Point 4	-12	-8	33	-11.673	-9.014	33.037	0.327	-1.014	0.037	1.066
Average								**0.278**	**-1.514**	**-0.046**	**1.548**
Thin wall	Point 3	-8	-12.5	25	-7.913	-12.623	24.852	0.087	-0.123	-0.148	0.211
	Point 2	-9	-12.5	25	-9.33	-12.688	24.963	-0.330	-0.188	-0.037	0.382
	Point 1	-8.5	-12.5	24.5	-8.483	-13.076	24.473	0.017	-0.576	-0.027	0.577
Average								**-0.075**	**-0.296**	**-0.071**	**0.390**

Table A.10: Typical statistical overview for C2-after cut off.

Feature	Element	Nominal			Actual			Deviation			
		X	**Y**	**Z**	**X**	**Y**	**Z**	**dX**	**dY**	**dZ**	**dN**
Thick wall	Point 6	-12	-7.5	32.5	-11.823	-8.966	32.397	0.177	-1.466	-0.103	1.480
	Point 5	-12	-7	33	-11.685	-9.019	32.877	0.315	-2.019	-0.123	2.047
	Point 4	-12	-8	33	-11.805	-9.038	32.885	0.195	-1.038	-0.115	1.062
Average								**0.229**	**-1.508**	**-0.114**	**1.530**
Thin wall	Point 3	-8	-12.5	25	-8	-12.517	24.999	0.000	-0.017	-0.001	0.017
	Point 2	-9	-12.5	25	-9	-12.542	24.999	0.000	-0.042	-0.001	0.042
	Point 1	-8.5	-12.5	24.5	-8.5	-12.498	24.5	0.000	0.002	0.000	0.002
Average								**0.000**	**-0.019**	**-0.001**	**0.020**

Table A.11: Typical statistical overview for D1-before cut off.

Feature	Element	Nominal			Actual			Deviation			
		X	Y	Z	X	Y	Z	dX	dY	dZ	dN
Thick wall	Point 6	-12	-7.5	32.5	-11.116	-9.017	32.765	0.884	-1.517	0.265	1.776
	Point 5	-12	-7	33	-11.472	-6.913	35.095	0.528	0.087	2.095	2.162
	Point 4	-12	-8	33	-11.116	-9.017	32.765	0.884	-1.017	-0.235	1.368
Average								**0.765**	**-0.816**	**0.708**	**1.769**
Thin wall	Point 3	-8	-12.5	25	-7.991	-12.666	25.03	0.009	-0.166	0.030	0.169
	Point 2	-9	-12.5	25	-9	-12.692	25.019	0.000	-0.192	0.019	0.193
	Point 1	-8.5	-12.5	24.5	-8.372	-12.358	24.455	0.128	0.142	-0.045	0.196
Average								**0.046**	**-0.072**	**0.001**	**0.186**

Table A.12: Typical statistical overview for D1-after cut off.

Feature	Element	Nominal			Actual			Deviation			
		X	Y	Z	X	Y	Z	dX	dY	dZ	dN
Thick wall	Point 6	-12	-7.5	32.5	-11.878	-8.112	31.722	0.122	-0.612	-0.778	0.997
	Point 5	-12	-7	33	-11.912	-8.352	33.457	0.088	-1.352	0.457	1.430
	Point 4	-12	-8	33	-11.842	-8.49	32.912	0.158	-0.490	-0.088	0.522
Average								**0.123**	**-0.818**	**-0.136**	**0.983**
Thin wall	Point 3	-8	-12.5	25	-7.975	-11.911	24.873	0.025	0.589	-0.127	0.603
	Point 2	-9	-12.5	25	-9.063	-11.919	24.906	-0.063	0.581	-0.094	0.592
	Point 1	-8.5	-12.5	24.5	-8.56	-12.017	24.442	-0.060	0.483	-0.058	0.490
Average								**-0.033**	**0.551**	**-0.093**	**0.562**

Table A.13: Typical statistical overview for D2-before cut off.

Feature	Element	Nominal			Actual			Deviation			
		X	Y	Z	X	Y	Z	dX	dY	dZ	dN
Thick wall	Point 6	-12	-7.5	32.5	-11.284	-8.965	32.282	0.716	-1.465	-0.218	1.645
	Point 5	-12	-7	33	-11.809	-7.164	35.017	0.191	-0.164	2.017	2.033
	Point 4	-12	-8	33	-11.231	-8.967	33.626	0.769	-0.967	0.626	1.385
Average								**0.559**	**-0.865**	**0.808**	**1.688**
Thin wall	Point 3	-8	-12.5	25	-8.003	-12.429	25.004	-0.003	0.071	0.004	0.071
	Point 2	-9	-12.5	25	-9.001	-12.461	25.002	-0.001	0.039	0.002	0.039
	Point 1	-8.5	-12.5	24.5	-8.498	-12.416	24.561	0.002	0.084	0.061	0.104
Average								**-0.001**	**0.065**	**0.022**	**0.071**

Table A.14: Typical statistical overview for D2-after cut off.

Feature	Element	Nominal			Actual			Deviation			
		X	Y	Z	X	Y	Z	dX	dY	dZ	dN
Thick wall	Point 6	-12	-7.5	32.5	-11.868	-8.133	33.816	0.132	-0.633	1.316	1.466
	Point 5	-12	-7	33	-11.865	-6.24	33.816	0.135	0.760	0.816	1.123
	Point 4	-12	-8	33	-11.868	-8.133	33.309	0.132	-0.133	0.309	0.361
Average								**0.133**	**-0.002**	**0.814**	**0.984**
Thin wall	Point 3	-8	-12.5	25	-7.99	-11.935	25.05	0.010	0.565	0.050	0.567
	Point 2	-9	-12.5	25	-9.035	-12.361	25.17	-0.035	0.139	0.170	0.222
	Point 1	-8.5	-12.5	24.5	-8.705	-12.461	24.735	-0.205	0.039	0.235	0.314
Average								**-0.077**	**0.248**	**0.152**	**0.368**

Table A.15: Typical statistical overview for E1-before cut off.

Feature	Element	Nominal			Actual			Deviation			
		X	Y	Z	X	Y	Z	dX	dY	dZ	dN
Thick wall	Point 6	-12	-7.5	32.5	-11.717	-9.04	32.593	0.283	-1.540	0.093	1.569
	Point 5	-12	-7	33	-11.553	-7.236	34.984	0.447	-0.236	1.984	2.047
	Point 4	-12	-8	33	-11.686	-9.037	32.931	0.314	-1.037	-0.069	1.086
Average								**0.348**	**-0.938**	**0.669**	**1.567**
Thin wall	Point 3	-8	-12.5	25	-8.051	-12.708	24.968	-0.051	-0.208	-0.032	0.217
	Point 2	-9	-12.5	25	-9.167	-12.729	25.049	-0.167	-0.229	0.049	0.288
	Point 1	-8.5	-12.5	24.5	-8.548	-12.688	24.479	-0.048	-0.188	-0.021	0.195
Average								**-0.089**	**-0.208**	**-0.001**	**0.233**

Table A.16: Typical statistical overview for E1-after cut off.

Feature	Element	Nominal			Actual			Deviation			
		X	Y	Z	X	Y	Z	dX	dY	dZ	dN
Thick wall	Point 6	-12	-7.5	32.5	-11.949	-7.397	32.861	0.051	0.103	0.361	0.379
	Point 5	-12	-7	33	-11.955	-7.116	33.278	0.045	-0.116	0.278	0.305
	Point 4	-12	-8	33	-11.904	-8.14	32.465	0.096	-0.140	-0.535	0.561
Average								**0.064**	**-0.051**	**0.035**	**0.415**
Thin wall	Point 3	-8	-12.5	25	-8.039	-12.09	24.953	-0.039	0.410	-0.047	0.415
	Point 2	-9	-12.5	25	-9.106	-12.092	24.959	-0.106	0.408	-0.041	0.424
	Point 1	-8.5	-12.5	24.5	-8.523	-12.076	24.518	-0.023	0.424	0.018	0.425
Average								**-0.056**	**0.414**	**-0.023**	**0.421**

Table A.17: Typical statistical overview for E2-before cut off.

Feature	Element	Nominal			Actual			Deviation			
		X	Y	Z	X	Y	Z	dX	dY	dZ	dN
Thick wall	Point 6	-12	-7.5	32.5	-11.537	-9.024	32.502	0.463	-1.524	0.002	1.593
	Point 5	-12	-7	33	-11.694	-6.711	34.991	0.306	0.289	1.991	2.035
	Point 4	-12	-8	33	-11.573	-9.022	33.168	0.427	-1.022	0.168	1.120
Average								**0.399**	**-0.752**	**0.720**	**1.583**
Thin wall	Point 3	-8	-12.5	25	-8.141	-12.741	24.144	-0.141	-0.241	-0.856	0.900
	Point 2	-9	-12.5	25	-9.002	-12.741	24.97	-0.002	-0.241	-0.030	0.243
	Point 1	-8.5	-12.5	24.5	-8.511	-12.679	24.48	-0.011	-0.179	-0.020	0.180
Average								**-0.051**	**-0.220**	**-0.302**	**0.441**

Table A.18: Typical statistical overview for E2-after cut off.

Feature	Element	Nominal			Actual			Deviation			
		X	Y	Z	X	Y	Z	dX	dY	dZ	dN
Thick wall	Point 6	-12	-7.5	32.5	-11.915	-6.219	32.653	0.085	1.281	0.153	1.293
	Point 5	-12	-7	33	-11.915	-6.219	32.653	0.085	0.781	-0.347	0.859
	Point 4	-12	-8	33	-11.907	-8.814	33.501	0.093	-0.814	0.501	0.960
Average								**0.088**	**0.416**	**0.102**	**1.037**
Thin wall	Point 3	-8	-12.5	25	-8	-12.491	25	0.000	0.009	0.000	0.009
	Point 2	-9	-12.5	25	-9	-12.507	25	0.000	-0.007	0.000	0.007
	Point 1	-8.5	-12.5	24.5	-8.504	-12.459	24.498	-0.004	0.041	-0.002	0.041
Average								**-0.001**	**0.014**	**-0.001**	**0.019**

Table A.20: Typical statistical overview for F1-after cut off.

Feature	Element	Nominal			Actual			Deviation			
		X	**Y**	**Z**	**X**	**Y**	**Z**	**dX**	**dY**	**dZ**	**dN**
Thick wall	Point 6	-12	-7.5	32.5	-11.864	-9.008	32.619	0.136	-1.508	0.119	1.519
	Point 5	-12	-7	33	-11.918	-8.803	33.387	0.082	-1.803	0.387	1.846
	Point 4	-12	-8	33	-11.918	-8.803	33.387	0.082	-0.803	0.387	0.895
Average								**0.100**	**-1.371**	**0.298**	**1.420**
Thin wall	Point 3	-8	-12.5	25	-7.982	-12.254	25.016	0.018	0.246	0.016	0.247
	Point 2	-9	-12.5	25	-9.017	-12.217	24.983	-0.017	0.283	-0.017	0.284
	Point 1	-8.5	-12.5	24.5	-8.574	-12.228	24.52	-0.074	0.272	0.020	0.283
Average								**-0.024**	**0.267**	**0.006**	**0.271**

Table A.21: Typical statistical overview for F2-before cut off.

Feature	Element	Nominal			Actual			Deviation			
		X	**Y**	**Z**	**X**	**Y**	**Z**	**dX**	**dY**	**dZ**	**dN**
Thick wall	Point 6	-12	-7.5	32.5	-11.441	-9.036	32.608	0.559	-1.536	0.108	1.638
	Point 5	-12	-7	33	-11.656	-9.039	33.161	0.344	-2.039	0.161	2.074
	Point 4	-12	-8	33	-11.656	-9.039	33.161	0.344	-1.039	0.161	1.106
Average								**0.416**	**-1.538**	**0.143**	**1.606**
Thin wall	Point 3	-8	-12.5	25	-8.004	-12.637	24.985	-0.004	-0.137	-0.015	0.138
	Point 2	-9	-12.5	25	-9.079	-12.677	24.979	-0.079	-0.177	-0.021	0.195
	Point 1	-8.5	-12.5	24.5	-8.509	-12.623	24.491	-0.009	-0.123	-0.009	0.124
Average								**-0.031**	**-0.146**	**-0.015**	**0.152**

Table A.19: Typical statistical overview for F1-before cut off.

Feature	Element	Nominal			Actual			Deviation			
		X	**Y**	**Z**	**X**	**Y**	**Z**	**dX**	**dY**	**dZ**	**dN**
Thick wall	Point 6	-12	-7.5	32.5	-11.868	-9.039	32.52	0.132	-1.539	0.020	1.545
	Point 5	-12	-7	33	-11.767	-9.04	33.024	0.233	-2.040	0.024	2.053
	Point 4	-12	-8	33	-11.767	-9.04	33.024	0.233	-1.040	0.024	1.066
Average								**0.199**	**-1.540**	**0.023**	**1.555**
Thin wall	Point 3	-8	-12.5	25	-8.001	-12.715	24.988	-0.001	-0.215	-0.012	0.215
	Point 2	-9	-12.5	25	-9.114	-12.728	24.895	-0.114	-0.228	-0.105	0.276
	Point 1	-8.5	-12.5	24.5	-8.174	-12.71	24.909	0.326	-0.210	0.409	0.564
Average								**0.070**	**-0.218**	**0.097**	**0.352**

Table A.22: Typical statistical overview for F2-after cut off.

Feature	Element	Nominal			Actual			Deviation			
		X	**Y**	**Z**	**X**	**Y**	**Z**	**dX**	**dY**	**dZ**	**dN**
Thick wall	Point 6	-12	-7.5	32.5	-11.571	-9.049	32.756	0.429	-1.549	0.256	1.628
	Point 5	-12	-7	33	-11.592	-9.052	32.779	0.408	-2.052	-0.221	2.104
	Point 4	-12	-8	33	-11.617	-9.073	32.932	0.383	-1.073	-0.068	1.141
Average								**0.407**	**-1.558**	**-0.011**	**1.624**
Thin wall	Point 3	-8	-12.5	25	-8	-12.49	25.001	0.000	0.010	0.001	0.010
	Point 2	-9	-12.5	25	-9	-12.507	25	0.000	-0.007	0.000	0.007
	Point 1	-8.5	-12.5	24.5	-8.499	-12.461	24.503	0.001	0.039	0.003	0.039
Average								**0.000**	**0.014**	**0.001**	**0.019**

A.3 H13 Datasheet

Materialdatenblatt

Material Data Sheet

Tool Steel 1.2344 / A681 H13 / H13[1]

Allgemeines

Bauteile aus Werkzeugstahl wie 1.2344 (H13) zeichnen sich durch eine hohe Härte sowie guten Warmfestigkeiten und Warmverschleißwiderständen aus. Weitere legierungstypische Eigenschaften wie eine gute Wärmeleitfähigkeit und Warmrissunempfindlichkeit machen den Werkstoff nutzbar für Warmarbeitswerkzeuge, Strangpresswerkzeuge oder Druckgießwerkzeuge, die durch das SLM®-Verfahren mit integrierten Kühlkanälen ausgestattet werden können. Auch für Schmiedegesenke oder Werkzeuge für die Kunststoffverarbeitung ist der Werkstoff hervorragend geeignet. Die guten mechanischen Kennwerte von diesem Werkzeugstahl erlauben die Verwendung an stark belasteten Einsatzorten, da durch die gute Verschleißfestigkeit die Abnutzung minimiert wird.

General

Components made of tool steel such as 1.2344 (H13) are known for great hardness combined with high ductility. Through selective application of alloying components, the material properties can be precisely adjusted. Applications for corrosion resistant alloys are found in medical technologies, the automotive industry as well as in aerospace engineering. Tool steel is mainly used for producing tools and molds. Its layered structure enables components to be equipped with integrated cooling channels. The good mechanical characteristic values of tool and stainless steel make it suitable for use in places that are exposed to heavy strain, because its high wear to resistance keeps abrasion to a minimum.

Materialaufbau

Bauteile aus H13 weisen nach dem Aufbau mit dem SLM® Verfahren ein homogenes, nahezu porenfreies Gefüge auf, wodurch die mechanischen Kennwerte im Bereich der Materialspezifikation liegen. Da der relativ hohe Kohlenstoffgehalt in der Legierung die notwendige Schweißbarkeit für den SLM®-Prozess einschränkt, können Mikrorisse im Gefüge nicht vollständig ausgeschlossen werden. Durch eine anschließende Nachbehandlung wie Wärmebehandeln (z.B. Spannungsarmglühen, Härten + Anlassen), können die Bauteileigenschaften an die individuellen Bedürfnisse angepasst werden.

Material Structure

SLM®-processed tool steel components exhibit a homogeneous, nearly non-porous texture, with mechanical characteristic values in the range of material specifications. Through subsequent processing such as heat treatment (e.g. precipitation hardening, soft annealing), the components' properties can be adapted to meet specific requirements.

Materialdatenblatt

Material Data Sheet

Tool Steel 1.2344 / A681 H13 / H13[1]

Physikalische und chemische Eigenschaften
Physical and Chemical Properties

Massendichte[2] Mass density[2]	≈ 8,0 g/cm³		
Schichtdicke Layer thickness	30 µm[3]	50 µm[4]	
Bauteildichte[5] Component density[5]	≈ 99,5 %	≈ 99,5 %	
Theoretische Aufbaurate je Laser[6] Theoretical build-up rate per laser[6]	10,4 cm³/h	15,6 cm³/h	
Chemische Zusammensetzung [Massenanteil in %][7] Chemical composition [Mass fraction in %][7]	Element	Min.	Max.
	Fe	Balance	Balance
	C	0,32	0,45
	Cr	4,75	5,50
	Mn	0,20	0,60
	Mo	1,10	1,75
	Ni + Cu		0,75
	P		0,03
	S		0,03
	Si	0,80	1,25
	V	0,80	1,20
Partikelgröße[7] Particle size[7]	10 – 45 µm		
Partikelform[8] Particle shape[8]	Sphärisch Spherical		

Materialdatenblatt
Material Data Sheet

Tool Steel 1.2344 / A681 H13 / H13[1]

Mechanische Kennwerte
Mechanical Data

Schichtdicke 30 µm[3] Layer thickness 30 µm[3]			Wie gebaut As-built		Wärmebehandelt[12] Heat-treated[12]	
M: Mittelwert Mean SD: Standardabweichung Standard deviation			M	SD	M	SD
Zugprüfung[9] **Tensile test[9]**						
Zugfestigkeit Tensile strength	R_m [MPa]	0° 90°	1244 1360	106 86	1719 1720	239 99
Dehngrenze Offset yield strength	$R_{p0,2}$ [MPa]	0° 90°	987 -	39 -	1528 -	32 -
Bruchdehnung Fraction strain	A [%]	0° 90°	2 1	2 2	4 9	2 2
Brucheinschnürung Reduction of area	Z [%]	0° 90°	- -	- -	14 16	5 5
Elastizitätsmodul Young's modulus	E [GPa]	0° 90°	203 -	23 -	- -	- -

Materialdatenblatt

Material Data Sheet

Tool Steel 1.2344 / A681 H13 / H13[1]

Die Eigenschaften und mechanischen Kennwerte gelten für von SLM Solutions geprüftes und vertriebenes Pulver, das mittels der Original-Parameter von SLM Solutions auf den Maschinen von SLM Solutions gemäß der jeweils gültigen Bedienungsanleitung (inklusive Installationsbedingungen und Wartung) verarbeitet wurde. Die Bestimmung der Bauteileigenschaften erfolgt gemäß angegebener Vorgehensweisen. Weitere Details zu den von SLM Solutions verwendeten Vorgehensweisen sind auf Anfrage erhältlich.

Die Angaben entsprechen unserem Kenntnis- und Erfahrungsstand zum Zeitpunkt der Veröffentlichung und bilden für sich allein keine ausreichende Grundlage für eine Bauteilauslegung. Bestimmte Eigenschaften von Produkten oder Bauteilen oder die Eignung von Produkten oder Bauteilen für spezifische Anwendungen werden nicht garantiert. Der Hersteller von Produkten oder Bauteilen ist für die qualifizierte Überprüfung der Eigenschaften und der Eignung für konkrete Anwendungen verantwortlich. Der Hersteller von Produkten oder Bauteilen ist verantwortlich für die Wahrung möglicher Schutzrechte Dritter sowie bestehender Gesetze und Bestimmungen.

The properties and mechanical characteristics apply to powder that is tested and sold by SLM Solutions, and that has been processed on SLM Solutions machines using the original SLM Solutions parameters in compliance with the applicable operating instructions (including installation conditions and maintenance). The part properties are determined based on specified procedures. More details about the procedures used by SLM Solutions are available upon request.

The specifications correspond to the most recent knowledge and experience available to us at the time of publication and do not form a sufficient basis for component design on their own. Certain properties of products or parts or the suitability of products or parts for specific applications are not guaranteed. The manufacturer of the products or parts is responsible for the qualified verification of the properties and their suitability for specific applications. The manufacturer of the products or parts is responsible for protecting any third party proprietary rights as well as existing laws and regulations.

DEUTSCHLAND ■ ÖSTERREICH ■ FRANKREICH ■ ITALIEN ■ USA ■ SINGAPUR ■ RUSSLAND ■ INDIEN ■ CHINA

SLM Solutions Group AG | Estlandring 4 | 23560 Lübeck | Deutschland
Fon +49 451 4060-3000 | Fax +49 451 4060-3250 | www.slm-solutions.com

Materialdatenblatt
Material Data Sheet

Tool Steel 1.2344 / A681 H13 / H13[1]

[1] Material gemäß ASTM A681 H13.
Material according to ASTM A681 H13.

[2] Materialdichte variiert im Rahmen der möglichen Variationen der chemischen Zusammensetzung.
Material density varies within the range of possible chemical composition variations.

[3] Materialdatei: H13_SLM_MBP2.2_30_FS_Stripes_T200_400W_V5103
Material data file: H13_SLM_MBP2.2_30_FS_Stripes_T200_400W_V5103

[4] Materialdatei: H13_SLM_MBP2.2_50_Stripes_T200_400W_V5103
Material data file: H13_SLM_MBP2.2_50_Stripes_T200_400W_V5103

[5] Optische Dichtebestimmung mittels Lichtmikroskopie.
Optical density determination by light microscopy.

[6] Theoretische Aufbaurate je Laser = Schichtdicke x Scangeschwindigkeit x Spurabstand.
Theoretical build-up rate for each laser = layer thickness x scan speed x track distance.

[7] Bzgl. pulverförmigen Ausgangsmaterials.
With respect to powder material.

[8] Gemäß DIN EN ISO 3252:2001.
According to DIN EN ISO 3252:2001

[9] Zugprüfung gemäß DIN EN ISO 6892-1:2017 B (DIN 50125:2016 – B6x30); Ausrichtung: 0°, 90°; Prüfmaschine: Zwick 1484; Lastbereich: 200 kN; Prüfgeschwindigkeit 0,008 1/s; Prüftemperatur: Raumtemperatur; Prüflabor: EWIS GmbH. Die Proben sind vor dem Zugversuch abgedreht worden.
Tensile test according to DIN EN ISO 6892-1:2017 B (DIN 50125:2016 – B6x30); orientation: 0°, 90°; testing machine: Zwick 1484; load range: 200 kN; testing speed: 0,008 1/s; testing temperature: room temperature; test laboratory: EWIS GmbH. Test samples were turned before tensile test.

[10] Härteprüfung gemäß DIN EN ISO 6507-1:2018.
Hardness testing according to DIN EN ISO 6507-1:2018.

[11] Rauheitsmessung gemäß DIN EN ISO 4288:1998; λc = 0,8 mm.
Roughness measurement according to DIN EN ISO 4288:1998; λc = 0,8 mm.

[12] Wärmebehandlung: Vorwärmen auf 750 °C für 2 h, anschließendes Austenitisieren bei 1050 °C für 15 min. und Abschrecken in ca. 60 °C warmen Öl. Sofortiges zweimaliges Anlassen bei 300 °C für 2,5 h mit Zwischenkühlung auf Raumtemperatur.
Heat treatment: preheating to 750 °C for 2 h, followed by austenitizing at 1050 °C for 15 min. and quenching in warm oil (about 60 °C). Immediate double tempering at 300 °C for 2.5 h with interstage cooling down to room temperature.

DEUTSCHLAND ■ ÖSTERREICH ■ FRANKREICH ■ ITALIEN ■ USA ■ SINGAPUR ■ RUSSLAND ■ INDIEN ■ CHINA

SLM Solutions Group AG | Estlandring 4 | 23560 Lübeck | Deutschland
Fon +49 451 4060-3000 | Fax +49 451 4060-3250 | www.slm-solutions.com